Chaotic mixing and transport in Rossby-wave critical layers

Article

Published Version

J. Fluid Mech. (1997), *vol.* 334, *pp.* 315–351

Chaotic mixing and transport in Rossby-wave critical layers

By KEITH NGAN AND THEODORE G. SHEPHERD
Department of Physics, University of Toronto, Toronto, M5S 1A7 Canada

(Received 27 July 1995 and in revised form 6 August 1996)

A simple, dynamically consistent model of mixing and transport in Rossby-wave critical layers is obtained from the well-known Stewartson–Warn–Warn (SWW) solution of Rossby-wave critical-layer theory. The SWW solution is thought to be a useful conceptual model of Rossby-wave breaking in the stratosphere. Chaotic advection in the model is a consequence of the interaction between a stationary and a transient Rossby wave.

Mixing and transport are characterized separately with a number of quantitative diagnostics (e.g. mean-square dispersion, lobe dynamics, and spectral moments), and with particular emphasis on the dynamics of the tracer field itself. The parameter dependences of the diagnostics are examined: transport tends to increase monotonically with increasing perturbation amplitude whereas mixing does not. The robustness of the results is investigated by stochastically perturbing the transient-wave phase speed. The two-wave chaotic advection model is contrasted with a stochastic single-wave model. It is shown that the effects of chaotic advection cannot be captured by stochasticity alone.

1. Introduction

The mixing and transport of tracer is a subject of great importance in many branches of fluid dynamics. In applications, the subject has traditionally been approached by appealing to an analogy between the kinetic motion of molecules and the eddy motion of fluid parcels. This leads to a flux–gradient relation wherein the flux of tracer by eddy motions is linearly related to the mean tracer gradient. As has long been appreciated, however, flux–gradient relations, when applied to fluid dynamics, have many deficiencies (see e.g. Tennekes & Lumley 1972; McIntyre 1992, §10). Most notably, the separation of scales that exists in kinetic theory between the length scale characterizing the (microscopic) transporting mechanism (i.e. the mean-free path) and that characterizing the (macroscopic) mean tracer gradient may not exist (Corrsin 1974). In atmospheric dynamics, the most spectacular example of the failure of the flux–gradient relation is the wintertime Antarctic stratospheric polar vortex (e.g. McIntyre 1989): the spatial scale of the eddy motion is much greater than the scale of the tracer gradients, and the tracer flux is smallest where the tracer gradient is largest.

An alternative approach to mixing and transport is offered by chaotic advection (e.g. Aref 1984; Ottino 1989). Chaotic advection, which has received considerable attention in recent years, describes a situation wherein regular Eulerian velocity fields yield chaotic particle trajectories. For two-dimensional incompressible flow, the

equations of motion for the particle trajectories constitute a Hamiltonian system and methods from Hamiltonian dynamical systems theory (e.g. MacKay & Meiss 1987) can be used. The phase-space geometry of these systems consists of regular and chaotic regions. In the case of time-periodic or 1.5 degree-of-freedom systems, regular regions are composed of invariant tori, which act as barriers to transport; these invariant tori are destroyed in chaotic regions, where there is also enhanced mixing. This kind of spatial inhomogeneity, in particular the occurrence of transport barriers, has much in common with the observed behaviour of tracers in geophysical fluids.

Chaotic advection has been extensively studied in the context of low-Reynolds-number Stokes flow (e.g. Aref & Balachandar 1986; Chaiken *et al.* 1986; Jana, Metcalfe & Ottino 1994). In these studies time dependence in the (Eulerian) velocity field is generated through motion of the boundaries: typically the boundary velocities alternate between several distinct values. A mixing 'protocol' is defined by the (instantaneous) boundary velocities and by the duration of time for which they are maintained. Because of the Stokes flow condition, transient effects are negligible and the velocity field is determined instantaneously by the boundary motion: it is externally specified, i.e. generated kinematically. Although weak transience can be studied within this framework (see Dutta & Chevray 1995), the relevance of chaotic advection to a situation in which the velocity is not externally imposed remains to be established. As chaotic advection models are inherently kinematical – effectively, the stream function must be prescribed – an important question is whether such models, when applied to dynamically generated phenomena, are consistent with the full dynamics: are they dynamically consistent?

In geophysical fluid dynamics, there have been several previous applications of chaotic advection to dynamically generated phenomena. Most of these applications have utilized 'two-wave' models, where the stream function (equivalently, the Hamiltonian) is given by the superposition of a stationary and a travelling wave, i.e.

$$\psi(x, y, t) = \psi_0(x, y) + \varepsilon\psi_1(x, y, t), \tag{1.1}$$

where ε is a small perturbation parameter and ψ_1 is periodic in t. In this way the perturbation is a continuous function of time; for geophysical phenomena this is more plausible than the discontinuous variations of the Stokes flow studies. The first two-wave model was that of Weiss & Knobloch (1989), who showed, using bifurcation theory, that the stream function for binary fluid convection is of the above form near the secondary bifurcation from travelling to modulated waves. Their model, despite its kinematical form, is a direct consequence of the full dynamical equations, and is thus dynamically consistent (near the secondary bifurcation).

The problem with two-wave models is that they will generally not be consistent with the full dynamics. Unlike the Stokes flow studies, where any imposed velocity field is physically realizable, in most geophysical applications one cannot arbitrarily impose a velocity field. Dynamical consistency has indeed been a problem with the (inviscid) studies that have followed Weiss & Knobloch (1989) – work by Cox *et al.* (1990) on chaotic advection by Rossby-like waves, Pierrehumbert (1991*a*,*b*) on modulated Rossby waves,† Samelson (1992) on Gulf Stream meanders, and del-Castillo-Negrete & Morrison (1993) (hereafter referred to as DM) on Rossby

† Pierrehumbert (1991*b*) also performed some dynamically consistent simulations of the two-dimensional Euler equations. However, the velocity field was not time-periodic, and of course could not be represented analytically.

waves in shear. These models are completely kinematic; they are derived from heuristic arguments and not from the governing equations.

The dynamical consistency problem may be seen in the following way. For two-dimensional vorticity-conserving fluids, the vorticity $q = \mathscr{L}(\psi)$, where $\mathscr{L}$ is a differential operator on the stream function ψ; therefore, if ψ is time-periodic, then q is time-periodic as well and chaotic advection is possible only when the vorticity field has already been homogenized (cf. Pierrehumbert 1991*a* and DM) – a constraint which cannot be satisfied except in special cases such as irrotational flow (Cox *et al.* 1990), or the flow around a Kida vortex (Polvani & Wisdom 1990). There is thus a fundamental discrepancy between these chaotic advection models and the two-dimensional vorticity-conserving fluids they are intended to describe (unless one restricts attention to flow regimes where the vorticity can be regarded as piecewise constant). The problem is particularly serious if one is interested in transport across a strong (potential) vorticity gradient, as, for example, occurs along the edge of the stratospheric polar vortex.

Nonetheless, time-periodic two-wave models merit further consideration. They are conceptually elegant and the physical mechanism underlying them should be robust. But if they are to be applied to large-scale, high-Reynolds-number, geophysical flows, where the (potential) vorticity is materially conserved to a good approximation on time scales well in excess of the eddy turnaround time, how then is this contradiction between periodic velocity fields and chaotic vorticity fields to be resolved? As has been articulated most clearly by Pierrehumbert (1991*b*) and Samelson (1996), periodic velocity fields *can* coexist with chaotic vorticity fields if there exists a separation of scales between the coarse- and fine-grained vorticity. If the velocity is dominantly associated with the coarse-grained vorticity, then the fine-grained vorticity is essentially decoupled from the velocity. This means that the fine-grained vorticity can behave as a (chaotic) passive tracer and that a dynamically consistent model can be constructed.

This viewpoint can be made mathematically precise within the context of critical-layer theory. Critical-layer theory (e.g. Stewartson 1981; Maslowe 1986) describes what happens in the vicinity of critical lines, where the difference between the basic-state velocity and the phase speed of a wave is small and where, for sufficiently weak viscosity, nonlinear effects are important. Such regions are of great physical importance because there is strong mixing and transport in (perturbed) critical layers. The Stewartson–Warn–Warn (SWW) solution, which describes the nonlinear development of a forced Rossby-wave critical layer in an inviscid linear shear flow (Stewartson 1978; Warn & Warn 1978), forms the basis of our model. The SWW solution has recently attracted interest because it is thought to be a useful conceptual model of Rossby-wave breaking events in the stratosphere (e.g. Juckes & McIntyre 1987): large-amplitude, quasi-stationary, upward-propagating Rossby waves break in the stratosphere, leading to a region of intense mixing and the formation of a 'surf zone' (McIntyre & Palmer 1983). There is increasing evidence that much (if not most) of the mixing in the vicinity of the stratospheric polar vortex takes place near stagnation points of the flow (e.g. Polvani & Plumb 1992), around critical lines in particular (Bowman 1996). Also, preliminary studies suggest that chaotic advection occurs outside the vortex (Pierce & Fairlie 1993; Bowman 1993), and occasionally, inside the vortex as well (Waugh *et al.* 1994).

Stewartson and Warn & Warn showed that with certain assumptions about the flow, there exists a special solution for which, to leading order in the wave amplitude: (i) the absolute vorticity in the inner critical-layer region behaves exactly like a passive tracer; and (ii) the changing absolute vorticity in the critical layer affects the

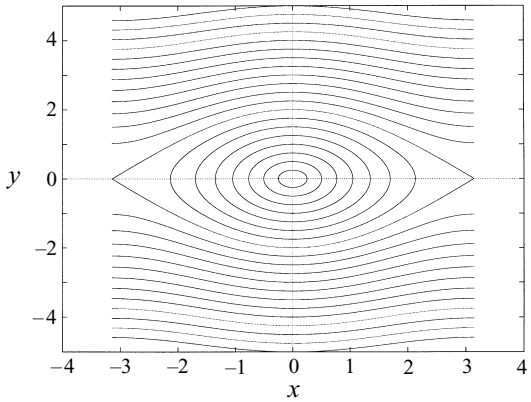

FIGURE 1. Unperturbed phase space geometry (i.e. streamlines of the SWW solution). A separatrix divides the inner (closed) orbits from the outer (open) orbits.

distribution in the outer region but does not react back upon itself. At this order, the absolute vorticity is advected by a steady stream function $\Psi_0 = -\frac{1}{2}y^2 + \cos x$ and the equations of motion for a tracer particle with coordinates $\big(x_i(t), y_i(t)\big)$ are

$$\dot{x}_i = -\frac{\partial \Psi_0}{\partial y_i}, \quad \dot{y}_i = \frac{\partial \Psi_0}{\partial x_i}. \tag{1.2}$$

Equation (1.2) describes a cat's eye or nonlinear resonance (see figure 1), the prototypical phase-space geometry of nonlinear dynamics. With the identification $(x, y, \Psi_0) \rightarrow (q, p, -H)$, the phase space is identical to the physical space and Hamilton's equations for a nonlinear pendulum are recovered.

For the SWW solution, absolute vorticity contours wrap up inside the cat's eye (see figure 2 of Killworth & McIntyre 1985), but the filaments remain distinct: there is stirring, not mixing (cf. Wiggins 1988), in the sense that small-scale structure is developed but not homogenized.† There is no transport, in any meaningful sense, because the entire phase space is partitioned by invariant curves; an important manifestation of this is that the inner (closed) contours are divided from the outer (open) contours by a separatrix.

Our model is obtained by perturbing the SWW solution with a time-dependent travelling wave, which produces chaotic advection: tracer trajectories are no longer constrained to follow steady vorticity isolines. Mixing occurs because distant tracer particles can be repeatedly brought together and dispersed (stretching and folding) in chaotic regions; transport occurs because tracers can be displaced meridionally where the invariant tori have been destroyed. Furthermore, in chaotic regions particle trajectories separate from one another at an exponential rate (the separation is merely algebraic in regular regions).

It can be shown that within the critical layer, the model's vorticity field remains decoupled from the advecting stream function. There can thus be chaotic mixing and transport even when the vorticity field has not been homogenized; the model is dynamically consistent to leading order. Pierrehumbert (1991*b*) was the first to suggest that the SWW solution could be used in a chaotic advection model.

† Of course in the long-time limit stirring leads to homogenization – and thus mixing – at any given scale; nevertheless, the distinction is clear enough for finite times. In the absence of diffusion, homogenization is to be associated with coarse-graining of the tracer field.

This paper is primarily concerned with a quantitative characterization of mixing and transport in this two-wave model. For the purposes of this work we associate mixing (in the absence of diffusion) with the *homogenization* (in a coarse-grained sense) of small-scale structure† and distinguish it from stirring, which is to be associated with the *development* of small-scale structure. More general definitions exist (see Aref 1991 for a lucid discussion), but the sense in which we use these terms is consistent with the conventional definition (again neglecting diffusion) that stirring refers to an increase in the amount of interfacial surface area whereas mixing refers to the redistribution of tracer across these surfaces; this is referred to as Eckart's definition in Aref (1991). We define transport to be the organized movement of tracer (e.g. across a specified boundary).

It must be said that we still lack a comprehensive theoretical framework in which to understand mixing and transport. There is at present no way in which the initial tracer distribution can be taken fully into account. For representative initial distributions we utilize a number of diagnostics in order to characterize mixing and transport separately. Our approach differs from most previous chaotic advection studies in that it emphasizes the tracer field rather than the stretching field (see e.g. Muzzio, Swanson & Ottino 1991); in geophysical applications, it is often convenient to diagnose mixing and transport directly from the tracer field. It is also because of the geophysical orientation of this work that mixing and transport are characterized separately – this is not an important issue in Stokes flow studies, where the domains are bounded and the particle trajectories are usually far from being regular.

The paper is organized as follows. In § 2, the model is presented, its dynamical consistency considered, and a preliminary analysis based on the resonance overlap criterion carried out. In § 3 transport is characterized: lobe dynamics (see Wiggins 1992) and brute-force computations are used to quantify the rate of transport; the mean-square dispersion of an initial distribution is used to quantify its spatial extent. In § 4 mixing is characterized: two-point spatial correlation functions are used as a proxy for the tracer spacing, and from them, tracer spectra and spectral moments are computed. In § 5, parameter dependences of mixing and transport are considered and compared with predictions from the Melnikov function. Stochastic perturbations are introduced in § 6 and their effect on mixing and transport is contrasted with deterministic chaotic advection. We conclude the paper with a Discussion in § 7.

2. The two-wave model

2.1. *Derivation*

Rossby-wave critical-layer theory describes what happens when monochromatic Rossby waves impinge upon a critical line. Without loss of generality for a barotropic flow, the Rossby waves can be taken to be stationary (i.e. with phase speed $c = 0$). At the 'northern' boundary $y = y_0 > 0$, an imposed stream function perturbation $\phi = a \cos mx$ generates southward-propagating Rossby waves of amplitude a. There is a critical line at $y = c = 0$, and $\phi \to 0$ as $y \to -\infty$. The stream function is obtained using the method of matched asymptotic expansions, and the SWW solution is a special case. Our model is a variant of the SWW solution wherein the advecting stream function contains a travelling-wave component but the vorticity remains a passive tracer to leading order.

† By small-scale structure we simply mean tracer structure that occurs at scales smaller than the characteristic (Eulerian) velocity scale.

The SWW solution is described in Appendix A. It yields the stream function (A 9), namely

$$\Psi_0 = -\tfrac{1}{2}Y^2 + \cos x, \tag{2.1}$$

where Y is a stretched meridional coordinate. The SWW solution is remarkable because, to leading order in the stationary-wave amplitude ϵ: (i) the vorticity distribution inside the critical layer, q, behaves exactly like a passive tracer for it is completely decoupled from the advecting stream function Ψ_0; and (ii) Ψ_0 is steady even though q is not.

With this single-wave stream function, tracers are constrained to follow streamlines, and, as discussed previously, there is neither mixing nor any meaningful transport. For there to be efficient mixing and transport, the advecting stream function must contain a time-dependent component. We choose to introduce time dependence in the stream function through a transient Rossby wave (i.e. a travelling wave). This is done by modifying the northern boundary condition to

$$\phi = a\cos x + a\varepsilon\cos k(x - \hat{c}t) \quad \text{at } y = y_o, \quad \varepsilon < 1\,. \tag{2.2}$$

(Note that the transient-wave amplitude ε is to be distinguished from the stationary-wave amplitude ϵ, and that here and henceforth Y and $\tau = \epsilon^{1/2}t$ are replaced with y and t.) With this new boundary condition, the derivation outlined in Appendix A proceeds as before with (A 5) replaced by

$$-\pi A Y_1(2y_o^{1/2}) + BJ_1(2y_o^{1/2}) = \frac{a}{y_o^{1/2}}\left[\cos x + \varepsilon\cos k(x - ct)\right], \tag{2.3}$$

where $c = \hat{c}/\epsilon^{1/2}$. After non-dimensionalizing time, the advecting stream function is given by

$$\Psi_0 = -\tfrac{1}{2}y^2 + \cos x + \varepsilon\cos k(x - ct) \tag{2.4}$$

in place of (A 9). Although there is nonlinear behaviour inside the critical layer, the forcing can, for small ε, be developed as a linear superposition because the dynamics outside the critical layer are linear at leading order (cf. Killworth & McIntyre 1985).

Equations (A 8) and (2.4) define the two-wave model. In exactly the same way as the SWW solution, its vorticity and velocity fields are decoupled; the vorticity does not need to be homogeneous for there to be chaotic mixing and transport. The critical-layer framework (which includes assumptions (A 3) and (A 7)) does, as anticipated, yield a model in which the small-scale vorticity is passively advected by the large-scale flow. Tracer (i.e. particle) trajectories are, of course, determined by (1.2).

Tracer evolution in the two-wave model and in the SWW solution are compared in figure 2. SWW flow is a case in which tracer is stirred, but not mixed.

Critical lines have been discussed in at least one previous chaotic advection study. In DM, the dynamical consistency problem is partially resolved by the fact that, by construction, the meridional gradient of the *basic-state* absolute vorticity q_o vanishes at the critical lines (i.e. $\mathrm{d}q_o(y)/\mathrm{d}y = 0$ at $y = c_i$, c_i being the phase speed of the ith mode).† Our model, through its multiple-scale formalism and weakly nonlinear dynamics, provides a natural extension of DM's analysis. It does not, however, completely circumvent the dynamical consistency problem because it is only correct to leading order in the perturbation amplitude.

† DM consider regular neutral mode solutions to a Bickley jet.

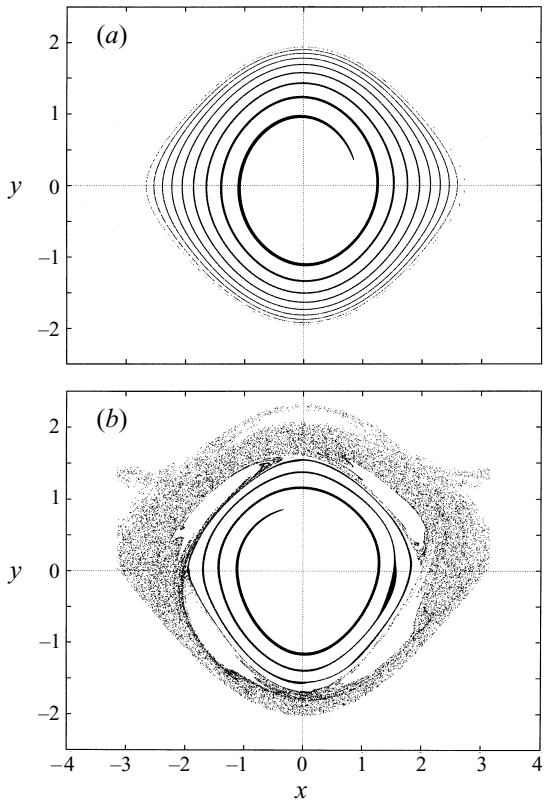

FIGURE 2. A comparison of the tracer evolution after 64 iterations (i.e. periods of the transient wave) for (*a*) the SWW solution and (*b*) the two-wave model with $\varepsilon = 0.1$, $k = 1$, $c = 3$. The initial distribution consists of 50 000 points in $[-0.5, 0.5] \times [1, 2]$. (*a*) exhibits pure stirring; (*b*) is a combination of stirring and mixing.

2.2. *Preliminary analysis: resonance overlap*

The SWW solution's domain is unbounded in x, but for our model it is convenient to impose periodic boundary conditions. This is permissible as the equations of motion

$$\dot{x}_i = y_i\,, \qquad \dot{y}_i = -\sin x_i - \varepsilon k \sin k(x_i - ct) \tag{2.5}$$

are invariant under translations of $\pm 2\pi$ in x if k is an integer.

With periodic boundary conditions, the hyperbolic fixed points for $\varepsilon = 0$ are given by $(x, y) = (\pm\pi, 0)$. For $\varepsilon \neq 0$, the dynamics are time dependent and it is necessary to work on a Poincaré section. A Poincaré section for a time-periodic system is defined by an initial choice of time t_0 and a map $\boldsymbol{x}(t_0 + nT) \rightarrow \boldsymbol{x}(t_0 + (n+1)T)$, where $T = 2\pi/kc$. If $t_0 = 0$, the fixed points $(x, y) = (\pm\pi, 0)$ persist. Linearizing around these fixed points, one can easily show that they will remain hyperbolic:

$$\forall\varepsilon, \quad k = \pm 1, \pm 3 \ldots\,; \qquad \forall\varepsilon < 1/k^2,\ k = \pm 2, \pm 4 \ldots\ . \tag{2.6}$$

For $\varepsilon = 0$, the stable manifold of one hyperbolic fixed point coincides with the unstable manifold of the other, forming a separatrix (e.g. Wiggins 1990) given by

$$y_{sep} = \pm 2^{1/2}(1 + \cos x)^{1/2}\,. \tag{2.7}$$

In figure 3, Poincaré sections are plotted for $k = 1$, $c = 3$ and $\varepsilon = 0.01$, 0.1 and

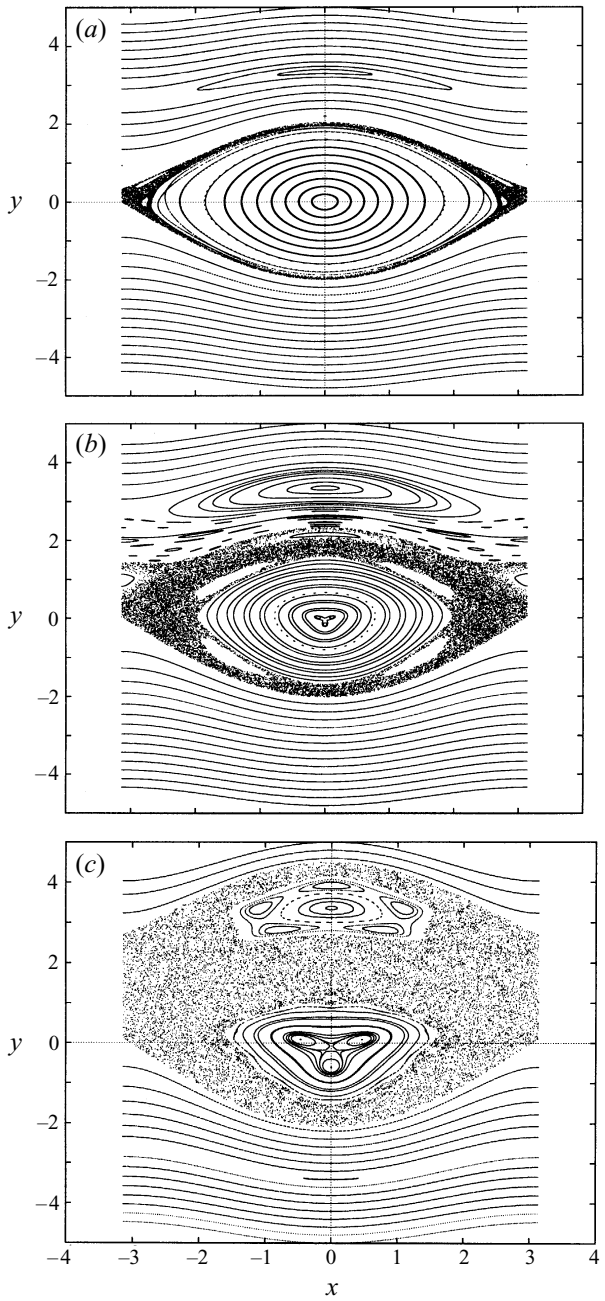

FIGURE 3. Poincaré sections for $k = 1$ and $c = 3$ for (*a*) $\varepsilon = 0.01$, (*b*) $\varepsilon = 0.1$, and (*c*) $\varepsilon = 0.4$. The width of the chaotic region increases with ε, and the secondary cat's eye results from the transient-wave perturbation.

0.4. Comparing these figures with that for the unperturbed solution (figure 1), one sees that the separatrix has split apart and that there is a chaotic layer surrounding it. Whereas all the orbits in figure 1 are regular, there are now many chaotic orbits. These orbits wander unpredictably in phase space within a region delimited by

invariant tori, regular trajectories that persist under the perturbation. The width of the chaotic layer increases markedly with ε. The simultaneous presence of regular and chaotic orbits is a characteristic feature of chaotic advection models; it corresponds to the physical fact that mixing and transport are spatially inhomogeneous. In the stratosphere, for example, there is very strong mixing in certain regions as well as barriers to transport at the edge of the polar vortex and in the subtropics (Polvani, Waugh & Plumb 1995).

The other notable feature about figure 3 is that there are now two cat's eyes, a somewhat smaller cat's eye having appeared around the line $y = 3$. Each wave component creates a cat's eye around $y = c_i$, where c_i is the phase speed of the corresponding wave. For a single isolated wave, i.e. $\Psi_0 = -\frac{1}{2}y^2 + \cos k_i(x - c_i t)$, the equations of motion in a co-moving frame with new variables $(\overline{x}, \overline{y}) = (x - c_i t,\ y)$ are

$$\dot{\overline{x}} = \overline{y} - c_i\,, \qquad \dot{\overline{y}} = -k_i \sin k_i \overline{x}\,,$$

and it follows that there will be a resonance (i.e. a critical layer) around $y = c_i$. Because of nonlinear interactions between the waves, however, the phase space is not composed only of regular orbits and unperturbed cat's eyes. Most prominently, trajectories near the separatrices – those most sensitive to perturbations – are smeared out in a chaotic layer.

A crude criterion for large-scale chaos (the destruction of all invariant tori between the resonances) is that the unperturbed separatrices touch; this is the resonance overlap criterion (r.o.c.) of Chirikov (see e.g. Lichtenberg & Lieberman 1992). The r.o.c. is discussed at length in DM. Applying the r.o.c. to our model, we obtain the following condition for large-scale chaos:

$$2(\varepsilon^{1/2} + 1) > |\, c_2 - c_1 \,| = |\, c \,|\,. \tag{2.8}$$

This predicts that with $c = 3$, there will be large-scale chaos for $\varepsilon = 0.4$ but not for $\varepsilon = 0.1$, as is observed in figure 3.

A symplectic integration algorithm (e.g. Yoshida 1990) has been used for all numerical computations. Unlike conventional schemes such as fourth-order Runge–Kutta, symplectic schemes preserve the symplectic structure of a Hamiltonian system; for two-dimensional canonical systems, this means that phase-space area will be conserved. Symplectic schemes also have very good error properties: even for large time steps, they do not usually show any secular drift in the energy. We have employed a fourth-order scheme due to McLachlan (1995).

Some of the calculations have been repeated with a fourth-order Runge–Kutta. While this leads, for larger values of the time step, to the smearing of some invariant tori, mixing and transport are nonetheless captured quite well.

3. Transport

With respect to transport, a useful distinction can be made between the rate of transport and its spatial extent. The rate of transport is determined by measuring the transport across a particular boundary (a local diagnostic), its spatial extent by the breadth of the tracer distribution (a global diagnostic). We shall mostly concentrate on the transport rate. In two-dimensional Hamiltonian systems, tracers are bounded by invariant tori so the extent of transport is not so useful a diagnostic.

Lobe dynamics (e.g. Wiggins 1992) is the starting point for our analysis. It provides an exact description of phase-space transport across perturbed separatrices in two-dimensional area-preserving maps. It is based on the fact that the stable and unstable manifolds of the map's hyperbolic fixed points must obey certain geometrical constraints. From these constraints, transport across the perturbed separatrix may be described in terms of the Poincaré-map iterates of a special set of lobes formed by the perturbed stable and unstable manifolds, the 'turnstile'. Lobe dynamics does not provide a definitive description of transport, but with its connection to the model's geometrical structure (which is ultimately responsible for stretching and folding), it is in a sense a fundamental one. It also provides useful insights into the mechanisms responsible for transport (e.g. tracers can only be transported across the perturbed separatrix if they intersect the turnstile).

For our purposes lobe dynamics is essentially a numerical method. Approximate analytical methods have recently been developed (Rom-Kedar 1994), but we do not make use of them. The relevance of lobe dynamics to our work is that it yields numerical results that can be a benchmark for later comparison (see the brute-force calculations below). Four basic steps are required in a numerical implementation. (i) The stable and unstable manifolds must be computed. (ii) Boundaries are defined as a union of the stable manifold of one fixed point and the unstable manifold of the other. For convenience, the two halves of the boundary are joined at the point $x = 0$. (See figure 4.) The regions so defined are labelled R1, R2 and R3, and points initially in region i are referred to as species i. The notion of different 'species' is simply a convenient way of incorporating information about the initial distribution of the tracers. (iii) The turnstile lobes must be located. These are lobes that conduct tracers across the separatrix; turnstile $L_{i,j}(1)$ conducts tracer from region i to j. Because the map is orientation preserving, lobes are mapped in the 'leap-frog' manner indicated by figure 4, and it follows that lobes can be mapped from the interior (R2) to the exterior (R1 and R3) and vice versa: this constitutes transport. (iv) The turnstile lobes are iterated forward in time and transport quantities are computed from intersections of the images with the turnstiles. Lobe dynamics was first applied to fluid dynamics by Rom-Kedar, Leonard & Wiggins (1990) (hereinafter referred to as RLW).

At all times, the total transport from region i to j after one iteration of the Poincaré map is given by the area of turnstile $L_{i,j}(1)$ – this is denoted by $\mu\big(L_{i,j}(1)\big)$, which is a constant. But a more interesting quantity is the net transport of a species i into region j during a specified Poincaré iterate n: $a_{i,j}(n)$, a flux. Letting $f^m\big(L_{i,j}(1)\big)$ represent the m-fold action of the Poincaré map on a turnstile, the transport of species 1 and 3 into the cat's eye is then given by

$$\begin{aligned} a_{1,2}(n) = \mu\Big(L_{1,2}(1)\Big) + \sum_{m=1}^{n-1} \Bigg[& \mu\Big(L_{1,2}(1) \bigcap f^m\Big(L_{1,2}(1)\Big)\Big) - \mu\Big(L_{1,2}(1) \bigcap f^m\Big(L_{2,1}(1)\Big)\Big) \\ & + \mu\Big(L_{2,1}(1) \bigcap f^m\Big(L_{2,1}(1)\Big)\Big) - \mu\Big(L_{2,1}(1) \bigcap f^m\Big(L_{1,2}(1)\Big)\Big) \\ & + \mu\Big(L_{3,2}(1) \bigcap f^m\Big(L_{1,2}(1)\Big)\Big) - \mu\Big(L_{3,2}(1) \bigcap f^m\Big(L_{2,1}(1)\Big)\Big) \\ & + \mu\Big(L_{2,3}(1) \bigcap f^m\Big(L_{2,1}(1)\Big)\Big) - \mu\Big(L_{2,3}(1) \bigcap f^m\Big(L_{1,2}(1)\Big)\Big) \Bigg], \end{aligned} \tag{3.1a}$$

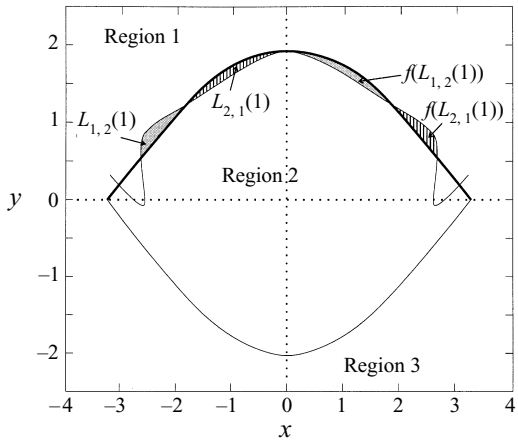

FIGURE 4. Configuration of the stable and unstable manifolds for $\varepsilon = 0.1$, $k = 1$, $c = 3$. The northern boundary is drawn with thick lines. Region 1 is north of the boundaries, region 3 south, and region 2 inside. The lobes formed by the manifolds are labelled $L_{i,j}(n)$, meaning that tracers are conducted from region i to j after n iterations of the Poincaré map. The lobes are mapped by the action of the Poincaré map in a 'leap-frog' manner: stippled areas are mapped to stippled areas, hatched areas to hatched areas. The lobes $L_{1,2}(1)$ and $L_{2,1}(1)$ are referred to as turnstile lobes.

$$a_{3,2}(n) = \mu\Big(L_{3,2}(1)\Big) + \sum_{m=1}^{n-1}\Bigg[\mu\Big(L_{3,2}(1)\bigcap f^m\Big(L_{3,2}(1)\Big)\Big) - \mu\Big(L_{3,2}(1)\bigcap f^m\Big(L_{2,3}(1)\Big)\Big)$$
$$+\mu\Big(L_{2,3}(1)\bigcap f^m\Big(L_{2,3}(1)\Big)\Big) - \mu\Big(L_{2,3}(1)\bigcap f^m\Big(L_{3,2}(1)\Big)\Big)$$
$$+\mu\Big(L_{1,2}(1)\bigcap f^m\Big(L_{3,2}(1)\Big)\Big) - \mu\Big(L_{1,2}(1)\bigcap f^m\Big(L_{2,3}(1)\Big)\Big)$$
$$+\mu\Big(L_{2,1}(1)\bigcap f^m\Big(L_{2,3}(1)\Big)\Big) - \mu\Big(L_{2,1}(1)\bigcap f^m\Big(L_{3,2}(1)\Big)\Big)\Bigg]. \tag{3.1b}$$

(See Appendix B for details.) The transport of species 3 through the cat's eye is given by

$$a_{3,1}(n) = \sum_{m=1}^{n-1}\Bigg[\mu\Big(L_{2,1}(1)\bigcap f^m\Big(L_{3,2}(1)\Big)\Big) - \mu\Big(L_{2,1}(1)\bigcap f^m\Big(L_{2,3}(1)\Big)\Big)$$
$$+\mu\Big(L_{1,2}(1)\bigcap f^m\Big(L_{2,3}(1)\Big)\Big) - \mu\Big(L_{1,2}(1)\bigcap f^m\Big(L_{3,2}(1)\Big)\Big)\Bigg]. \tag{3.2}$$

For the cases we will be considering, $a_{1,3}(n)$ and $a_{3,1}(n)$ are found to be identically zero. By conservation of area and conservation of species, it then follows that

$$a_{2,1}(n) = a_{1,2}(n), \qquad a_{2,3}(n) = a_{3,2}(n). \tag{3.3}$$

Transport into the cat's eye equals transport out.

The transport expressions (3.1) are evaluated by placing a large number of points inside each turnstile lobe and iterating. Because of the tremendous stretching and distortion produced by the flow, it is not possible, as would ideally be the case, to follow the lobe boundaries directly (cf. RLW; Franjione & Ottino 1987). The present method is simple to understand and relatively straightforward to implement, though

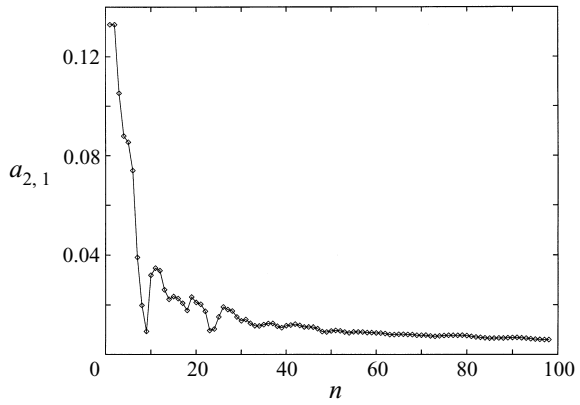

FIGURE 5. Lobe dynamics flux $a_{2,1}(n)$ for $\varepsilon = 0.1$, $k = 1$, $c = 3$. Approximately 50 000 points are used in the calculation. The maximum possible flux is given by the area of the turnstile lobe $L_{2,1}(1)$.

the determination of the manifolds and the lobes is not unambiguous. A set of points in the unstable linear eigenspace of each hyperbolic fixed point is iterated forward in time (e.g. Parker & Chua 1992) and a third-order B-spline routine is then used to interpolate between them. The initial set of points is chosen using the criterion that the lobe areas be extremal with respect to variations in the locations of the points along the linear eigenvectors. (An alternative method has also been used wherein the initial points have been chosen by a numerical search around the critical points, but this does not significantly alter the results.)

$a_{2,1}(n)$, the flux across the northern boundary of tracers initially inside the cat's eye, has been computed using approximately 50 000 points in each turnstile lobe (figure 5). The flux is initially constant because the turnstile $L_{2,1}(1)$ is completely filled with species 2 and tracers transported across the separatrix have yet to return. For $n \geqslant 3$, members of species 2 begin to be transported back across the boundary and the flux decreases rapidly. For large n, the tracer distribution is very distorted and it intersects the upper turnstiles alternately, leading to transport into and out of the cat's eye. The resulting fluctuations in the flux are therefore a kind of oscillation (cf. RLW). The tendency of the flux to approach zero as $n \to \infty$ is consistent with the tracer distribution approaching a well-dispersed state.

In figure 6(a), $a_{2,1}$ is plotted on log-log scales in order to examine how rapidly the flux goes to zero. A linear slope is indicative of power-law-type behaviour. There are two quasi-linear regimes: at early times ($1 < n < 7$), and at long times ($n > 10$). From a least-squares fit, $a_{2,1} \sim n^{-0.51\pm0.04}$ in the first regime, and $a_{2,1} \sim n^{-0.71\pm0.02}$ in the second. Summing the fluxes to obtain the cumulative transport, $T_{2,1}(n)$, of species 2 into region 1 as a function of time, there are two power-law regimes once more (figure 6b): $n^{0.77\pm0.01}$ and $n^{0.370\pm0.001}$. There is analogous behaviour for $\varepsilon = 0.01$. The occurrence of power-law regimes is noteworthy because it suggests a relationship with anomalous diffusion (cf. Young 1988). Note that these results are heavily dependent on the boundary conditions. Without periodic boundary conditions, there would be one-way transport out of the cat's eye (see Appendix B): tracers initially inside the cat's eye would be transported outside never to return.

$a_{2,3}$ is approximately constant for $\varepsilon = 0.1$ and $\varepsilon = 0.01$. Because the turnstile intersections are too small to be discerned by the numerical scheme, the time-dependence of $a_{2,3}$ is lost – it simply equals the area of the lower turnstile, $\mu\big(L_{2,3}(1)\big)$.

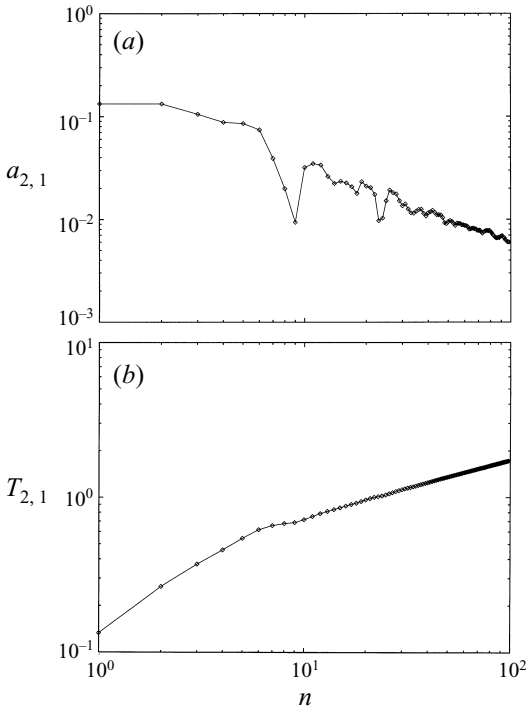

FIGURE 6. (*a*) $a_{2,1}(n)$ for $\varepsilon = 0.1$, $k = 1$, $c = 3$ plotted on log-log scales. A linear slope is indicative of power-law behaviour. (*b*) $T_{2,1}(n)$, the cumulative transport of species 2 into region 1, obtained by summing $a_{2,1}(n)$.

The smallness of the transport is consistent with the Poincaré sections (the lower separatrices do not exhibit any discernible splitting and the adjacent orbits are regular), and with the r.o.c. (the lower separatrix is much further from the secondary resonance). For these parameters, then, the lower turnstiles do not contribute to any meaningful transport; the results are virtually unchanged if the lower turnstile is ignored altogether.

The above results are robust: the fluxes are virtually unchanged when the number of points placed inside the turnstile or the time step are varied. This is further confirmed by a direct brute-force calculation wherein the fluxes are computed by counting the number of tracers crossing the perturbed separatrix for an initial distribution consisting of a large number of tracers inside region 2 (except for that portion bounded by invariant tori). Normalizing the fluxes with respect to $\mu(L_{2,1}(1))$, there is good agreement for $\varepsilon = 0.1$ (figure 7). Note, however, that without the lobe dynamics framework a much larger number of tracers must be followed, the vast majority of which do not initially lie inside the turnstile.

In lobe dynamics, a boundary defined by the perturbed stable and unstable manifolds is used to determine the initial distribution and the transport fluxes. It is thus of interest to consider other boundaries. A reasonable choice for an alternative boundary is the unperturbed separatrix. When the flux is measured across the unperturbed separatrix and the tracers are, as before, initially placed inside the perturbed separatrices, the agreement with lobe dynamics is very good. The flux in this case is insensitive to the precise location at which it is measured. But when the tracers are initially placed inside the unperturbed separatrices, there is quasi-uniform decay (figure 8). (This flux

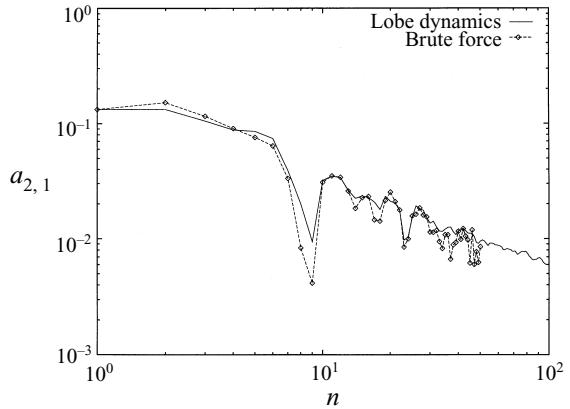

FIGURE 7. Brute-force computation of $a_{2,1}(n)$ for $\varepsilon = 0.1$, $k = 1$, $c = 3$ using approximately 500 000 points. There is good agreement with lobe dynamics. The brute-force flux is normalized with respect to $\mu(L_{2,1}(1))$.

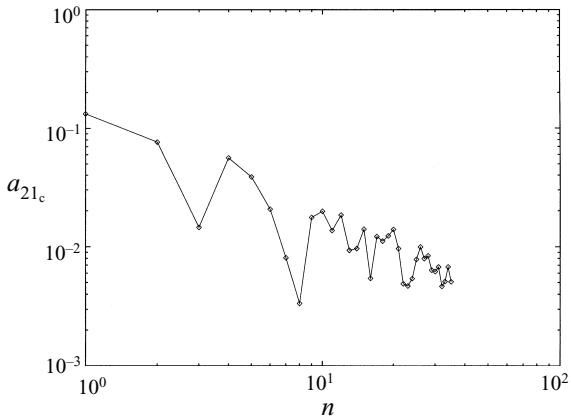

FIGURE 8. Brute-force flux across the unperturbed separatrix, a_{21c}, for $\varepsilon = 0.1$, $k = 1$, $c = 3$ using approximately 500 000 points. The initial distribution is bounded by the unperturbed separatrix and there is quasi-uniform decay. The flux is normalized with respect to $\mu(L_{2,1}(1))$.

is referred to as a_{21c}.) Previously, we observed two distinct regimes for $a_{2,1}$ because the initial distribution lies entirely to one side of the turnstile, and an adjustment stage is required to reach a quasi-equilibrium distribution. In contrast, the initial tracer distribution for a_{21c} straddles the turnstile and no adjustment stage can be discerned. Such rapid spatial variation in the transport properties violates one of the underlying assumptions of diffusive or flux–gradient behaviour (cf. Corrsin 1974).

Let us now consider the spatial extent of transport. The spatial extent of meridional transport is characterized by the mean-square dispersion in y,

$$\sigma^2 = \left\langle \Big(y - \langle y \rangle \Big)^2 \right\rangle, \tag{3.4}$$

where the angle brackets denote an average over the ensemble of particle positions. For an initial distribution straddling the turnstile, σ^2 increases rapidly for small n, and quickly levels off; but for an identical distribution located to the interior of the

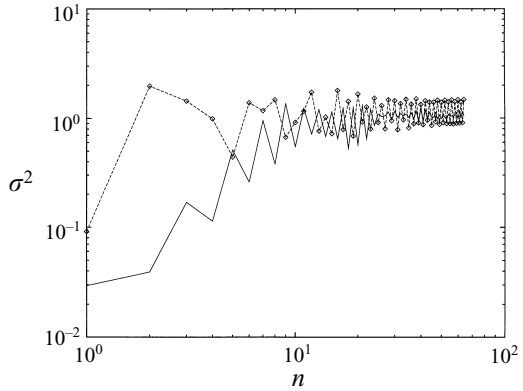

FIGURE 9. σ^2 vs. n for an initial distribution straddling the turnstile (dashed line + diamonds), and for an initial distribution to the interior of the turnstile (solid line). In both cases $\varepsilon = 0.1$, $k = 1$, $c = 3$. The initial distributions are $[-0.25, 0.25] \times [1.75, 2.25]$ and $[-0.25, 0.25] \times [1.25, 1.75]$, respectively. The initial rate of increase is strongly dependent on the initial distribution, but saturation with large n is observed in both cases.

turnstile, σ^2 increases much more slowly, taking a longer time to saturate (figure 9). The initial σ^2 for these two distributions is the same. In both cases there is saturation for large n because the existence of invariant tori in this 1.5 degree-of-freedom system prevents the meridional dispersion from increasing without bound; the saturation values are comparable because both initial distributions contain points in the same chaotic region.

The results of figure 9 highlight a couple of important differences with respect to diffusive behaviour. Most notably, there is a strong dependence on the initial distribution: the initial increase in σ^2 is much slower for the initial distribution lying entirely to one side of the turnstile. Also, the saturation of σ^2 is a completely non-diffusive effect. For a purely diffusive system, $\sigma^2 \sim t$.

These results are consistent with those obtained by Schoeberl & Bacmeister (1993) in computations of isentropic tracer trajectories from analysed stratospheric winds. They showed that the initial increase in the meridional dispersion depended on the orientation of the tracer field relative to the potential vorticity contours: the mean-square dispersion either increased rapidly and levelled off, or was nearly constant from the outset. Like our results, theirs indicate that transport depends crucially on the initial tracer distribution and that it can be markedly non-diffusive. However, the initial distribution of their non-dispersing cases consisted of tracers lying entirely within non-breaking potential vorticity contours (corresponding roughly to invariant tori); our calculations have been performed using initial distributions that, at least partly, lie inside the chaotic region.

σ^2 describes the variance of the tracers about the mean of the distribution. One could also examine the variance of the individual tracer displacements, i.e.

$$\tilde{\sigma}^2 = \left\langle \Big((y(t) - y(0)) - \langle y(t) - y(0) \rangle \Big)^2 \right\rangle. \tag{3.5}$$

σ^2 and $\tilde{\sigma}^2$ differ in the choice of origin; for random walks, they approach the same value as $n \to \infty$ (random displacements are independent of the initial position). For regular orbits, however, $\tilde{\sigma}^2$ will display periodic variations in the individual tracer

displacements that do not appear in σ^2, the latter being a measure of the ensemble variance. Consequently, we have used σ^2 rather than $\tilde{\sigma}^2$. (For the cases we have considered, σ^2 and $\tilde{\sigma}^2$ are indeed almost identical for large n.)

Mezić & Wiggins (1994) have shown that, under conditions of non-ergodicity, $\tilde{\sigma}^2$ asymptotically scales as t^2 for periodic coordinates. A similar condition applies to σ^2 for $n \to \infty$. This result does not apply here because y is not a periodic coordinate.

4. Mixing

We characterize mixing by the homogenization of small-scale structure in the tracer field. (As alluded to earlier, 'small-scale structure' refers to features in the tracer field that are smaller than the characteristic scale of the advecting velocity field, and 'homogenization' is to be interpreted in a coarse-grained sense.) The reason for this definition is that it captures the important idea that mixing is a dynamical process. By this we simply mean that mixing cannot be determined from the instantaneous tracer field; rather, its time evolution must be studied. It thus follows that the diagnosis of mixing is highly dependent on the initial conditions and that it will show a marked scale dependence. A quantification of the spatial structure in some scale-dependent manner is required.

The problem of instantaneous characterization of a tracer field has been considered by Muzzio *et al.* (1991). (See Városi, Antonsen & Ott 1991 for another approach.) They propose two means by which mixing can be characterized: (i) a distribution of stretching values; and (ii) a distribution of striation thicknesses. Both of these are probability density functions. From the time evolution of these quantities, one can make inferences about the amount of mixing taking place. For technical reasons, Muzzio *et al.* (1991) chose to emphasize the distribution of stretching values. They showed that for properly randomized initial conditions, the distribution of stretching values obeys single-parameter scaling; and in a subsequent paper (Muzzio *et al.* 1992), that it may, after appropriate coarse-graining, obey multifractal scaling. However, the connection between stretching and mixing is less clear for domains without fixed boundaries, such as are relevant to geophysical applications. Furthermore, it is often the case that one has information on the tracer field but not the stretching field (i.e. the velocities). Thus we prefer to diagnose mixing directly from the tracer field.

When the tracer field is composed of discrete particles, as in this study, the natural analogue of the distribution of striation thicknesses is the distribution of interparticle separations. Following Pierrehumbert (1992), however, we opt for a spectral approach rather than one based on probability distribution functions. A spectral approach is useful because it has a clear physical interpretation. The progress of mixing at different scales and at different times is clearly visible.

Let $H(r)$ denote the distribution of tracer pairs lying within an interparticle separation r. (This is an integral from 0 to r of the distribution of interparticle separations.) Assuming that the tracer field is isotropic, it can be shown (Pierrehumbert 1992) that the isotropic power spectrum of the tracer distribution is of the form

$$C(\kappa) \sim \kappa \int_0^\infty \frac{\mathrm{d}H(r)}{\mathrm{d}r} J_0(\kappa r)\, \mathrm{d}r\,, \tag{4.1}$$

where J_0 is a zeroth-order Bessel function and κ is the spatial wavenumber. This expression is obtained after performing the angular integration of a continuous two-dimensional Fourier transform of the tracer distribution. In order to calculate this quantity numerically we discretize the interval $[0, r_{max}]$, where r_{max} is greater than the

maximum interparticle separation, into uniform divisions. In the runs described in this section, we have used $r_{max} = 8$ and 40 000 uniform divisions, and we consider only the first 200 modes. (The initial interparticle spacing corresponds to a wavenumber $\kappa \approx 4000$.)

There are several other technical points associated with the calculation of (4.1). First, the normalization is arbitrary. Rather than normalizing the amplitudes to unity, we simply normalize with respect to the number of tracer pairs. This is done because the time evolution of the spectra must be considered in order to diagnose mixing; consequently, a time-dependent normalization cannot be used. Second, in computing $C(\kappa)$, the number of tracer pairs increases quadratically with N. This places a strong constraint on the number of particles that can be followed, especially when multiple runs are required for each set of parameter values. Pierrehumbert (1994) has been able to compute tracer spectra for a much larger number of tracer particles by taking one-dimensional cuts of the tracer field.

An interesting question is the scaling of $C(\kappa)$ with κ. If there is an extensive scaling range for which $H(r) \sim r^D$ (D is the correlation dimension), then it is easily shown that (Pierrehumbert 1991*b*)

$$C(\kappa) \sim \kappa^{1-D} \tag{4.2}$$

and thus $C(\kappa) \sim \kappa^{-1}$ as $D \to 2$ (i.e. complete mixing of the tracer field).† The power spectrum of tracer fluctuations in homogeneous two-dimensional turbulence is conventionally expected to scale like κ^{-1} as well (e.g. Lesieur 1990). If, however, the tracer distribution is patchy, or has localized fine-scale structure, then steeper spectra are possible. This has been discussed by Saffman (1971) and Gilbert (1988) in the context of two-dimensional turbulence. This mechanism is one possible explanation for an approximately κ^{-2} spectrum found in both stratospheric measurements and numerical simulations (Strahan & Mahlman 1994; Sirovich, Everson & Manin 1995; Bacmeister *et al.* 1996).

In figure 10, $C(\kappa)$ is plotted against κ for $\varepsilon = 0$ and $\varepsilon = 0.1$, with n increasing geometrically from 1 to 64. The initial distribution consists of approximately 64 000 points inside $f(L_{2,1}(1))$. While the spectrum for $\varepsilon = 0$ asymptotes to κ^{-1}, beginning at intermediate scales and then extending to smaller scales, the spectrum for $\varepsilon = 0.1$ asymptotes uniformly over a broad range of scales to something steeper than κ^{-1}. (It lies between κ^{-1} and κ^{-2}.) This behaviour was also noted by Pierrehumbert (1991*b*). It is not clear whether the spectra will remain steeper than κ^{-1} as the discrete particle distribution approaches a continuous one and $t \to \infty$, although this is certainly plausible. Some speculations on this phenomenon are provided by Pierrehumbert (1994).

Other calculations have also been made with fewer points and divisions, with comparable results.

Looking more closely at the spectral evolution in figure 10, differences between the two cases become more apparent. We had previously characterized $\varepsilon = 0$ as a pure stirring case (i.e. stirring without any mixing), and $\varepsilon = 0.1$ as a mixing case (i.e. stirring first, then mixing). Let us now examine how these intuitive descriptions are reflected in the spectra. For $\varepsilon = 0$, the evolution is basically uniform and the spectrum shifts relatively smoothly to higher wavenumbers. Small scales are developed quickly, but their decay is gradual, reflecting the lack of homogenization in this integrable case. (This is in sharp contrast to pure diffusive behaviour, which would preferentially erode

† There are some subtleties associated with this limit (see Pierrehumbert 1992).

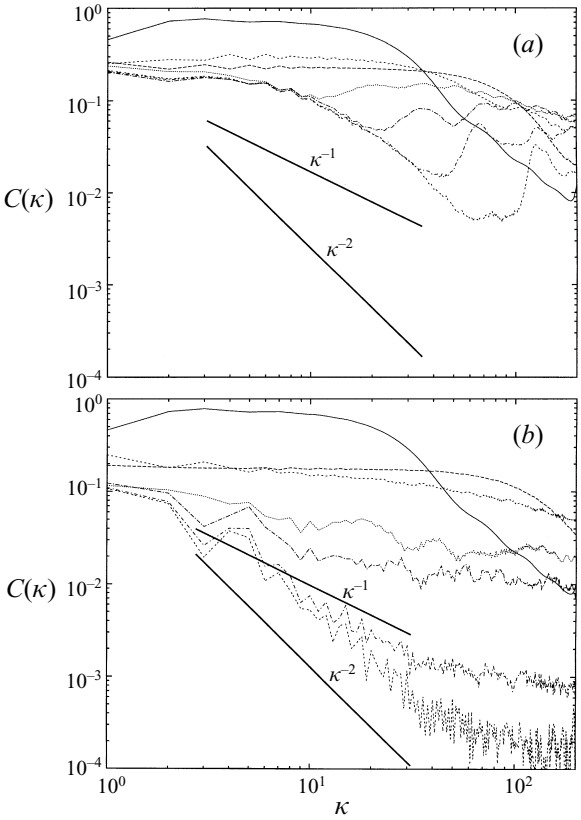

FIGURE 10. $C(\kappa)$ vs. κ for $n = 1$ to 64. (*a*) $\varepsilon = 0$ and (*b*) $\varepsilon = 0.1$, $k = 1$, $c = 3$. n increases by powers of two as one goes downwards. The initial distribution for both cases is identical and consists of 63 886 points inside $f(L_{2,1}(1))$ (for $\varepsilon = 0.1$, $k = 1$, $c = 3$). The spectrum is computed from $r = 0$ to $r = 8$ using 40 000 gridpoints.

the small scales.) For $\varepsilon = 0.1$, the behaviour is initially rather similar. Subsequently, however, there is a much stronger decay at smaller scales. We identify this decay with homogenization and mixing (in a coarse-grained sense). The fact that mixing occurs first at larger scales, and only later at smaller scales, is in striking contrast to diffusive behaviour (cf. Pierrehumbert 1991*b*).

The above analysis is largely qualitative in nature and it is predicated on our knowledge that $\varepsilon = 0$ corresponds to a stirring case and $\varepsilon = 0.1$ to a mixing case. In general this knowledge is not available *a priori* (for instance when we consider the parameter dependence); some representative quantitative diagnostics are required.

The features identified in the power spectra can be crudely quantified with spectral moments. By analogy with two-dimensional turbulence phenomenology (e.g. Pedlosky 1987, §3.28), the centroid of the tracer spectrum, K_1, and the dispersion about the centroid, Δ_{K-K_1}, are defined by

$$K_1 = \frac{\int_{\kappa_{min}}^{\kappa_{max}} \kappa C(\kappa)\,\mathrm{d}\kappa}{\int_{\kappa_{min}}^{\kappa_{max}} C(\kappa)\,\mathrm{d}\kappa}, \qquad \Delta_{K-K_1} = \frac{\int_{\kappa_{min}}^{\kappa_{max}} (\kappa - K_1)^2 C(\kappa)\,\mathrm{d}\kappa}{\int_{\kappa_{min}}^{\kappa_{max}} C(\kappa)\,\mathrm{d}\kappa}. \tag{4.3}$$

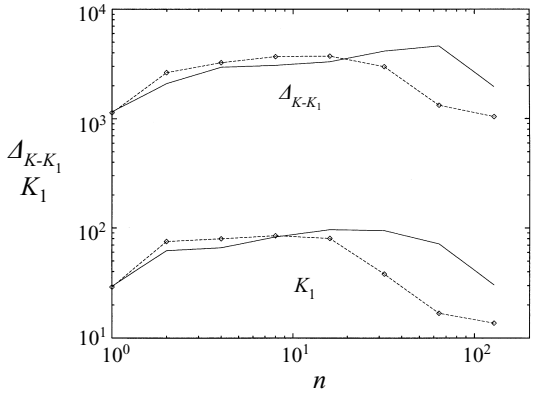

FIGURE 11. K_1 and Δ_{K-K_1} vs. n for the spectra of figure 10. $\varepsilon = 0$ (solid lines) and $\varepsilon = 0.1$, $k = 1$, $c = 3$ (dashed lines + diamonds).

The spectral moments are computed with $\kappa_{min} = 1$ and $\kappa_{max} = 200$. We expect that as small scales develop, K_1 will increase markedly, and that as small scales are homogenized, Δ_{K-K_1} will decrease markedly. In practice we have found the qualitative behaviour of both diagnostics to be similar in most cases.

In figure 11, K_1 and Δ_{K-K_1} are shown for $\varepsilon = 0$ and $\varepsilon = 0.1$. For $\varepsilon = 0$, the development of small-scale structure is prolonged relative to $\varepsilon = 0.1$. This is another illustration of the transient wave's effect on mixing. The diagnostics confirm that, at least in the context of the two-wave model, mixing can be viewed as a two-step process: (i) the development of small scales (reflected here in increasing K_1), and (ii) their subsequent homogenization (reflected here in decreasing Δ_{K-K_1}).

5. Parameter dependence

The last two sections have focused primarily on the parameters $\varepsilon = 0.1$, $k = 1$, $c = 3$; in this section we consider the parameter dependence of mixing and transport.

The parameter dependence of mixing and transport has not been extensively considered in previous chaotic advection studies. In Stokes flow studies, the emphasis has been on the optimization of mixing rather than on parameter dependence *per se* (cf. Jana *et al.* 1994). In the geophysical context, however, the parameter dependence of mixing and transport must be considered because one cannot restrict one's attention to a single set of parameters.

A Melnikov analysis is the simplest way to examine the parameter dependence of transport (see e.g. Samelson 1992), albeit only in the vicinity of the separatrix. The *total* transport across the perturbed separatrix is determined by the turnstile areas, and the turnstile areas may be estimated with the Melnikov function. While convenient, this approach is, however, only an approximate one. Apart from the approximate nature of the Melnikov function itself, the time-dependent nature of transport – and especially the role of the initial tracer distribution – is neglected.

The Melnikov function (e.g. Wiggins 1990; Drazin 1992) measures, on a specified Poincaré section, the separation between the stable and unstable manifolds connecting the hyperbolic fixed points. For the dynamical system

$$\dot{x} = f_1(x, y) + \varepsilon g_1(x, y, t), \qquad \dot{y} = f_2(x, y) + \varepsilon g_2(x, y, t), \tag{5.1}$$

where g_1, g_2 are periodic functions of time, the Melnikov function is given by an

ε	k	c	Measured area	Melnikov area	Difference (%)
0.01	1	3	0.0136 ± 0.0001	0.0135	1
0.1	1	3	0.1330 ± 0.0001	0.1354	2
0.1	1	2.5	0.2473 ± 0.0001	0.2476	0.1
0.1	3	3	0.0253 ± 0.0001	0.0252	0.4
0.2	1	3	0.2703 ± 0.0005	0.2710	0.3

TABLE 1. Turnstile lobe areas. The measured area is an average over several lobes (typically 3–5 lobes are used; see figure 4). The error is given by the standard deviation.

integral over the unperturbed separatrix $\boldsymbol{q}_0(t;t_0)$:

$$M(t_h;t_0) = \int_{-\infty}^{\infty} f\big(\boldsymbol{q}_0(t;t_0)\big) \wedge g\big(\boldsymbol{q}_0(t;t_0), t+t_h\big)\,\mathrm{d}t\,, \tag{5.2}$$

where t_0 denotes the phase of the Poincaré section, t_h parameterizes distance along the unperturbed separatrix, and '$\wedge$' denotes the wedge product $f \wedge g = f_1 g_2 - g_1 f_2$. The splitting between the manifolds is given by

$$d(t_h;t_0) = \varepsilon \frac{M(t_h;t_0)}{|\, f(\boldsymbol{q}_0(t_h;t_0))\,|} + O(\varepsilon^2). \tag{5.3}$$

Because the perturbation is time-periodic, the time interval between the primary intersection points of a given lobe, $t_{h2} - t_{h1}$, equals $T/2$, T being the period of the perturbation. For a specified Poincaré section, the area of a given lobe L can then be computed by integrating the Melnikov function from t_{h1} to t_{h2} (e.g. Wiggins 1992):

$$\mu(L) = \varepsilon \int_{t_{h1}}^{t_{h2}} |\, M(t_h)\,|\,\mathrm{d}t_h + O(\varepsilon^2)\,. \tag{5.4}$$

Repeating this procedure for different k and c, the parameter dependence of the total transport across the upper (or lower) separatrix can be estimated.

The Melnikov function for the upper separatrix of (2.5) may be written as

$$M(t_h) = \int_{-\infty}^{\infty} \frac{2}{\cosh t} \Bigg\{ -k \sin\Big[k\big(4\arctan(\mathrm{e}^t) - \pi\big)\Big] \cos kc(t+t_h) + k \cos\Big[k\big(4\arctan(\mathrm{e}^t) - \pi\big)\Big] \sin kc(t+t_h) \Bigg\} \mathrm{d}t\,. \tag{5.5}$$

(The Poincaré section is defined at times $t = n\pi$, and $\boldsymbol{q}_0(0)$ has been chosen to correspond to $(x, y) = (0, 2)$.) As a check, the lobe areas predicted by the Melnikov function are compared with a direct computation in table 1. The agreement is acceptable, even for relatively large values of ε.

Using this expression, $\mu(L)/\varepsilon$ is plotted against k (at fixed c) and against c (at fixed k) in figure 12. Except for large values of k and c, for which the Melnikov function is small, exponential decay is observed throughout the range of k and c. Exponential decay is significant because it suggests a particularly simple characterization of the parameter dependence.

With respect to the ε dependence, the Melnikov function predicts that the total transport is directly proportional to ε for small ε. It can be seen that $\sigma^2\,(n = 64)$ is a

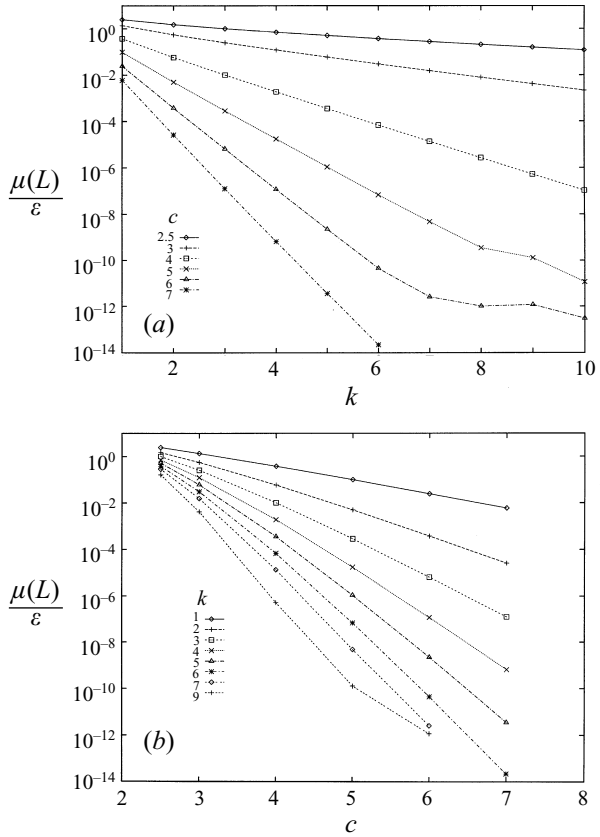

FIGURE 12. Variation of $\mu(L)/\varepsilon$ with (*a*) k (at fixed c) and with (*b*) c (at fixed k). There is exponential decay except for large k and c.

monotonic function of ε (figure 13), though a decidedly nonlinear one.† A nonlinear dependence of transport on perturbation amplitude was also found by Weiss (1991) for a travelling wave map.

One of the main results from our analysis of the rate and spatial extent of transport is that transport can show a non-trivial time dependence – there may exist early and late regimes. This kind of time dependence arises from the periodic boundary conditions and the initial tracer distribution; it cannot be captured by a Melnikov function alone. To illustrate this point, we now consider $T_{2,1}$, the cumulative transport of species 2 into region 1 (i.e. out of the cat's eye). $T_{2,1}$ is plotted against t for $k = 1$ and $k = 3$ in figure 14(*a*), with $\varepsilon = 0.1$ and $c = 3$ in both cases. A Melnikov analysis predicts that the ratio of these quantities is constant, namely

$$\frac{T_{2,1}(t;\varepsilon_i,\, k_i,\, c_i)}{T_{2,1}(t;\varepsilon_j,\, k_j,\, c_j)} = \frac{\mu(L;\varepsilon_i,\, k_i,\, c_i)}{\mu(L;\varepsilon_j,\, k_j,\, c_j)} \frac{T(\varepsilon_j,\, k_j,\, c_j)}{T(\varepsilon_i,\, k_i,\, c_i)}, \tag{5.6}$$

where $T(\varepsilon, k, c)$ is the period of the perturbation. This is clearly not the case: the

† In this and several subsequent figures, where parameter dependences are considered, the initial tracer distribution is defined by the lobe iterate $f(L_{2,1}(1))$ for a single value of ε, $\varepsilon = 0.1$. Since these figures correspond to long-time behaviour ($n = 64$), for which the tracer distribution is quasi-homogenized, we expect the choice of initial condition to be relatively unimportant. This has been confirmed using $f(L_{2,1}(1))$ for another value of ε, $\varepsilon = 0.2$.

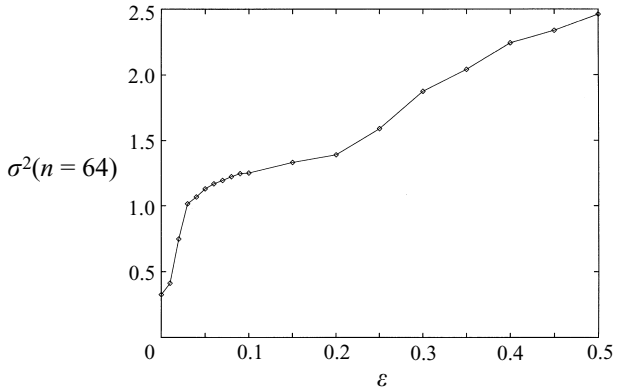

FIGURE 13. $\sigma^2(n = 64)$ vs. ε for $k = 1, c = 3$ using 63 886 points in $f(L_{2,1}(1))$ (for $\varepsilon = 0.1$). The mean-square dispersion varies monotonically, but nonlinearly, with ε.

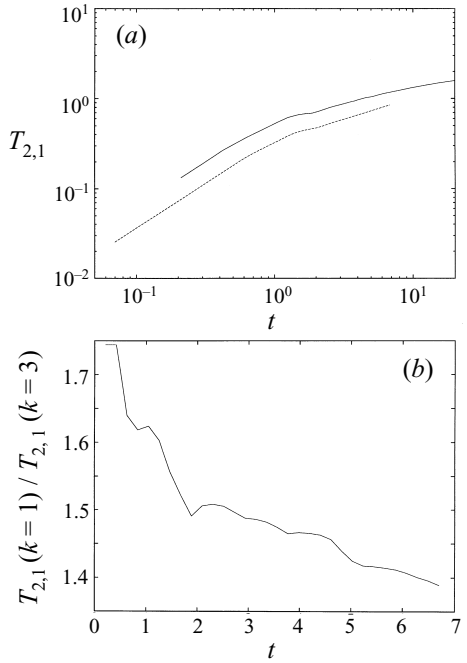

FIGURE 14. Effect of k on transport. (*a*) $T_{2,1}(t)$ for $k = 1$ (solid line) and $k = 3$ (dashed line). $\varepsilon = 0.1$ and $c = 3$ in both cases. Note that $T_{2,1}$ is plotted against t and not n. (*b*) $T_{2,1}(t; k = 1)/T_{2,1}(t; k = 3)$.

expression (5.6) is initially correct, but it begins to fail at longer times as the ratio of $T_{2,1}(k = 1)$ to $T_{2,1}(k = 3)$ decreases over the course of the integration (figure 14*b*). The transport of individual species need not follow the total transport (of phase space). While of obvious importance, the separatrix splitting is not – as was touched upon in §3 – the only factor influencing transport.

Perhaps the most serious limitation of the Melnikov function is that it does not directly relate to mixing. Strictly speaking, the separatrix splitting only applies to transport across the separatrix. It has, nevertheless, been suggested that in spite of its obvious limitations the Melnikov function is perhaps the best diagnostic for

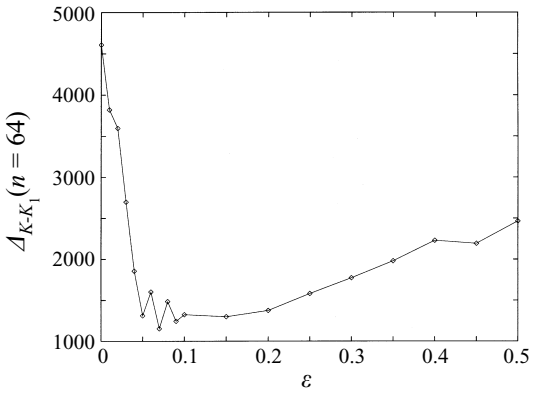

FIGURE 15. Variation of $\Delta_{K-K_1}(n = 64)$ with ε for $k = 1$ and $c = 3$. The initial distribution consists of 63 886 points inside $f(L_{2,1}(1))$ (for $\varepsilon = 0.1$). The dependence on ε is not monotonic.

determining the efficiency of mixing (Jana *et al.* 1994). That mixing can, however, exhibit a non-monotonic response to variations in the perturbation strength (and therefore in the Melnikov function) has been noted previously. In a study of the flow between two eccentrically rotating cylinders, Aref & Balachandar (1986) observed that, for given geometric parameters, mixing is maximized for a particular modulation frequency.

Direct numerical computations are required to determine the parameter dependence of mixing. To this end, Δ_{K-K_1} has been computed after 64 iterations for a range of ε values (figure 15). As expected, Δ_{K-K_1} does not change monotonically with ε: it decreases initially with ε, reaches a minimum around $\varepsilon = 0.07$, and increases from that point on. Recalling that small Δ_{K-K_1} is indicative of strong mixing (i.e. a nearly homogenized state), this suggests that there is indeed an optimal value of ε for which the mixing can be maximized, and that increasing the perturbation beyond this value diminishes the amount of mixing that occurs during a fixed time interval. These results are relatively robust to changes in the number of points and in the discretization.

This behaviour is the net result of two competing effects. One is that the stretching rate increases with ε; the other is that the size of the chaotic region also increases with ε (cf. figure 3). The first of these effects tends to increase the mixing, while the second tends to decrease it. Since the stretching rate will eventually saturate, one expects the mixing to be maximized for some value of ε. To see this, consider figure 16, where the ensemble-averaged finite-time (to $n = 64$) Liapunov exponent is plotted against ε. The slope of this plot decreases noticeably around $\varepsilon = 0.05$. Assuming that the size of the chaotic region grows linearly with ε for small ε – which is a reasonable assumption inasmuch as the lobe areas determined by the Melnikov function are quite good (table 1) – this is consistent with the mixing being maximized around $\varepsilon = 0.07$.

6. Noise

To this point, the parameters have all been constants. Time-dependent parameters constitute a natural extension of the two-wave model and should be considered. We have considered a particularly simple form for the time dependence: stochastic variation of the phase speed. In the stratosphere, for example, the period of transient waves is certainly not constant. Perturbations of this type are referred to as multi-

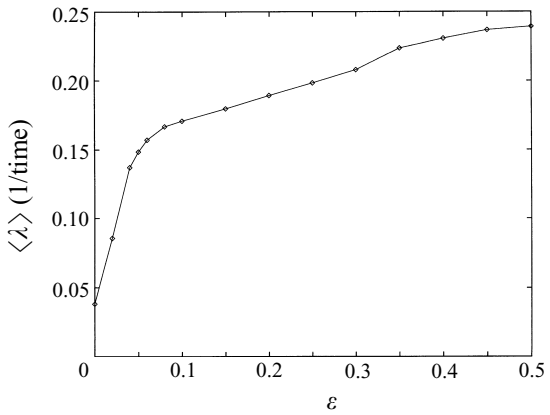

FIGURE 16. Ensemble-averaged finite-time Liapunov exponent $\langle\lambda\rangle$ vs. ε for $k = 1$, $c = 3$. An ensemble of 34 000 points initially lying inside $f(L_{2,1}(1))$ (for $\varepsilon = 0.1$) is used (the results are nearly identical for 64 000 points). The averages are computed after $n = 64$ iterations. The perturbed trajectory is initially displaced by an amount $\delta = 4 \times 10^{-7}$ in a random orientation, and the renormalization is done after every time step.

plicative noise (e.g. van Kampen 1981) and should be distinguished from additive noise, wherein a noise term is appended to the equations of motion. The effects of additive noise are better understood, but for nonlinear systems the introduction of additive noise may not be justifiable. Nonetheless, the introduction of multiplicative noise into the two-wave model is heuristic; it simply provides a test of the model's robustness and helps clarify the relationship between chaos, regular motion, and mixing.

We perturb an average phase speed c_0 with a noise term of amplitude δ_c, i.e.

$$\tilde{c} = c_0 + \tfrac{1}{2}\delta_c \eta\,, \tag{6.1}$$

where η is a stochastic variable in $[-1, 1]$ with a constant autocorrelation time τ, i.e. η changes values only at times $m\tau$ (where m is a positive integer). The system remains Hamiltonian with this stochastic perturbation, though there is a different Hamiltonian system after each interval of τ. Visually, the location of the secondary resonance shifts with the perturbation. The effects of this can be seen in the effective Poincaré section of figure 17, where the orbits are smeared out almost completely (cf. figure 3*b*).† Because invariant tori do not (formally) exist in stochastically perturbed systems, the tracers can now be carried much further in y.

Let us first examine some qualitative effects. In figure 18, both σ^2 and T_{21c}, the integrated flux out of the cat's eye, are seen to increase with decreasing τ. This is in accord with the naive expectation that the rate and extent of meridional transport increase monotonically with the stochastic perturbation. It is also consistent with the observation of Aref & Jones (1989) that (additive) noise tends to enhance particle separation. In figure 19, Δ_{K-K_1} is plotted against n for several values of τ. Here, decreasing τ leads to a much less rapid drop-off of Δ_{K-K_1} with time. This suggests that the mixing (at large times) decreases with decreasing τ. (The small reductions in Δ_{K-K_1} for small n are not relevant to mixing as we have defined it.)

† The smearing-out also reflects the fact that a Poincaré section is no longer well-defined because the period of the perturbation is not constant. This phenomenon is, nonetheless, real: the Poincaré sections are similar when ε is stochastically perturbed in place of c.

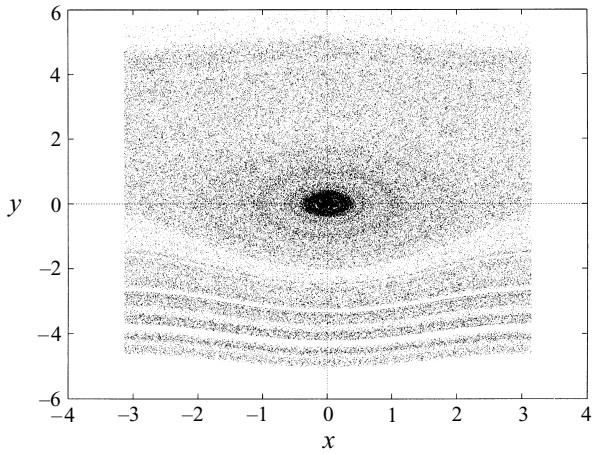

FIGURE 17. Effective Poincaré section for a stochastic perturbation to $\varepsilon = 0.1$, $k = 1$, $c = 3$: $\delta_c = 0.1, \tau = 3T$. Note that the smearing-out is almost complete.

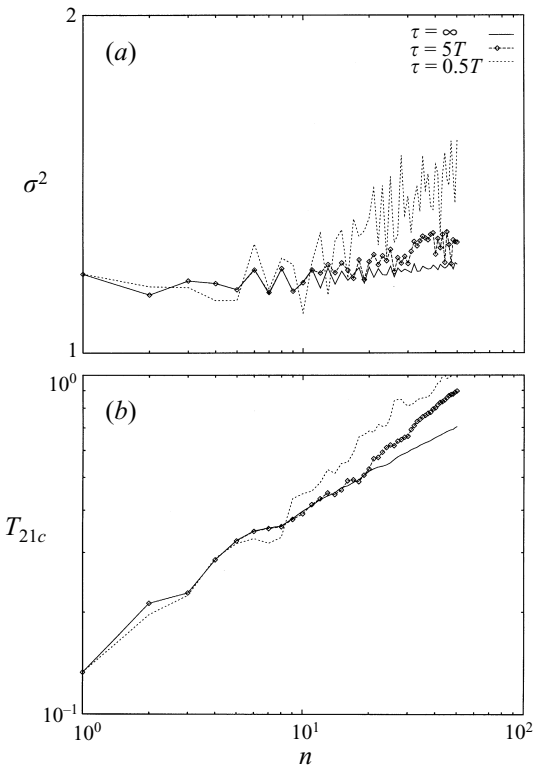

FIGURE 18. Qualitative effect of the autocorrelation time τ on transport. (*a*) σ^2 and (*b*) T_{21c} vs. n for $\varepsilon = 0.1$, $k = 1$, $c = 3$ and $\delta_c = 0.25$. Log-log scales are used in both cases. Transport increases as τ is reduced from ∞ (i.e. deterministic dynamics) to $5T$ and $0.5T$. The initial distribution consists of approximately 500 000 points inside the unperturbed separatrix. T_{21c} is computed by normalizing the fluxes with respect to $\mu(L_{2,1}(1))$.

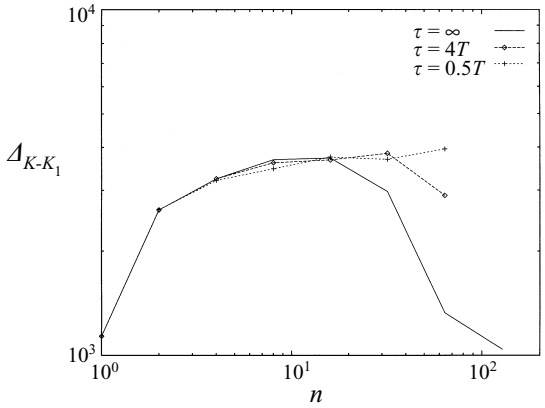

FIGURE 19. Qualitative effect of the autocorrelation time τ on mixing. Δ_{K-K_1} vs. n for $\varepsilon = 0.1$, $k = 1$, $c = 3$ and $\delta_c = 0.2$. Mixing decreases as τ is reduced from ∞ (i.e. deterministic dynamics) to $4T$ and $0.5T$. The initial distribution consists of 63 886 points inside $f(L_{2,1}(1))$ (for $\varepsilon = 0.1$ and $\delta_c = 0$).

At first sight, these results seem to be similar to those for the ε dependence (beyond the optimal-mixing value of ε): increasing stochasticity (i.e. decreasing τ) tends to increase transport, but decrease mixing. In fact, however, the parameter dependences of mixing and transport on ε and $1/\tau$ are different. Figure 20 shows the dependence of $\sigma^2(n = 64)$ and $\Delta_{K-K_1}(n = 64)$ on τ, based on average values from an ensemble of eight realizations. As $1/\tau$ is increased, σ^2 increases until $\tau \approx T$ (recall that T is the period of the travelling-wave perturbation), after which it decreases; on the other hand, Δ_{K-K_1} increases quasi-monotonically throughout. In contrast, when ε is increased (see figures 13 and 15), it is σ^2 that increases monotonically while Δ_{K-K_1} decreases and then increases. It is evident that chaotic advection and stochasticity are not equivalent, though their effects are qualitatively similar for weak stochasticity ($\tau \gg T$) and moderate ε. (Note that less mixing has occurred after 64 iterations for the stochastically perturbed case than for the unperturbed $\varepsilon = 0.1$ case (cf. figure 11).)

As with the ε dependence, it is instructive to examine the dependence on τ of the finite-time ensemble-averaged Liapunov exponent (figure 21). The stretching decreases steadily with increasing stochasticity, the decrease being greatest for $\tau < 2T$. Although it is true that the area of the 'chaotic region' is no longer precisely defined, it does (based on figure 20*a*) appear to increase with $1/\tau$, at least for $\tau > T$. This means that the competition between increasing stretching (which generally enhances mixing) and increasing size of the chaotic region (which generally diminishes mixing) seen in figure 15 is not present; here, the two effects are complementary and mixing decreases monotonically with τ. Indeed, it is this complementarity that explains why mixing is slower with the stochastically perturbed two-wave model than with the deterministic one for the same ε and n (cf. figure 11): the stretching for $\tau \in [0, 10T]$ is weaker (cf. figure 16), and the dispersion of tracer is greater (cf. figure 13). In other words, mixing is delayed in the stochastically perturbed two-wave model because the preceding development of small scales is slower. This is consistent with the notion that small scales tend to develop exponentially fast in chaotic advection models, but only algebraically fast in stochastic models.

Further insight into this behaviour may be gained by examining the spectral evolution of a single realization of the tracer field (figure 22). The shallowness of the spectra for large n is particularly striking.

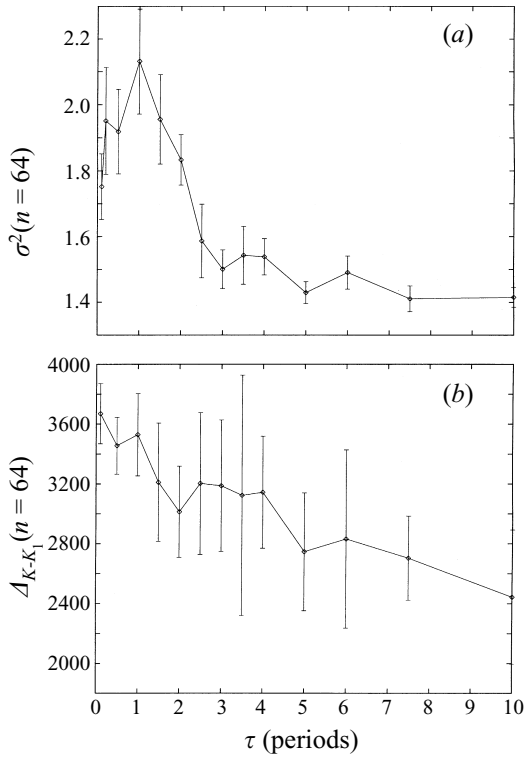

FIGURE 20. Variation of (*a*) $\sigma^2(n = 64)$ and (*b*) $\Delta_{K-K_1}(n = 64)$ with τ. $\varepsilon = 0.1$, $k = 1$, $c = 3$ and $\delta_c = 0.2$. The initial distribution consists of 33 709 points inside $f(L_{2,1}(1))$ (for $\varepsilon = 0.1$ and $\delta_c = 0$). The average values are determined from an ensemble of eight realizations; the error bars are given by the standard deviation. In (*b*), the spectrum is computed using interparticle separations from 0 to 8 on a grid of 40 000 points.

Another interesting feature about figure 20 is that the peak in $\sigma^2(n = 64)$ occurs at $\tau = T$. This is suggestive of stochastic resonance, a generic phenomenon in stochastically perturbed systems (e.g. Moss, Bulsara & Shlesinger 1993). We have confirmed, for several different values of k, c, and δ_c, that the peak in σ^2 always occurs around $\tau = T$. (Actually, the peaks have been found between $\tau = 0.7T$ and $\tau = 1.2T$.)

A comparison of the effects of stochasticity and (deterministic) chaotic advection in the two-wave model is made difficult by their mutual interaction. We thus consider a model wherein mixing is generated by stochasticity alone. This is done by adding multiplicative noise to the SWW solution, i.e.

$$\Psi_0 = -\tfrac{1}{2}y^2 + \cos(x - \tilde{c}t)\,. \tag{6.2}$$

Mixing in the stochastic single-wave model has been compared with mixing in the non-stochastic single-wave model ($\varepsilon = 0$) and the chaotic (but non-stochastic) two-wave model ($\varepsilon = 0.1, \delta_c = 0$) from $n = 1$ to 64 iterations (not shown). The development of small-scale structure is severely retarded (with respect to $\varepsilon = 0.1$) for the stochastically perturbed single wave, and the onset of homogenization is correspondingly delayed.

The parameter dependences of $\sigma^2(n = 64)$ and $\Delta_{K-K_1}(n = 64)$ (figure 23) are similar to those for the stochastically perturbed two-wave model (figure 20), except that there is now no sign of any drop in σ^2 for small τ. The behaviour is quasi-monotonic in

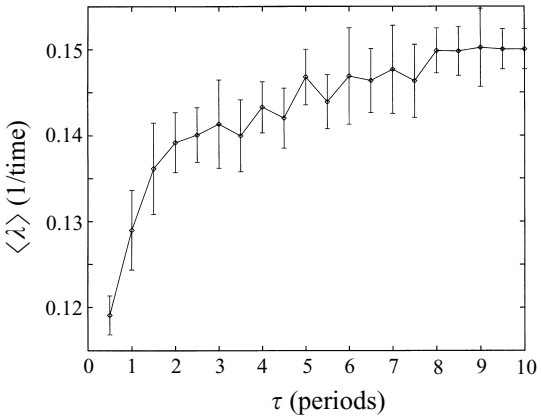

FIGURE 21. Ensemble-averaged finite-time Liapunov exponent $\langle\lambda\rangle$ for $\varepsilon = 0.1$, $k = 1$, $c = 3$, $\delta_c = 0.2$ and various τ. The averages are computed after $n = 64$ iterations from an ensemble of eight realizations, and the error bars are given by the standard deviation. Other details of the calculation are as in figure 16.

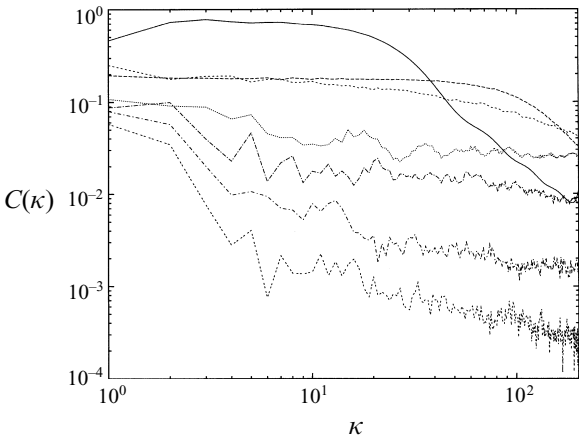

FIGURE 22. $C(\kappa)$ vs. κ for $n = 1$ to 64 for $\varepsilon = 0.1$, $k = 1$, $c = 3$ and $\delta_c = 0.2, \tau = 0.5T$. n increases by powers of two as one goes downwards. The initial distribution consists of 63 886 points inside $f(L_{2,1}(1))$ (for $\varepsilon = 0.1$ and $\delta_c = 0$) and 40 000 divisions are used; other details of the calculation are as in figure 10. Note the shallowness of the spectra.

both cases: with decreasing τ, mixing decreases while transport increases. (It is worth noting that the stochastically perturbed single-wave model is the only case we have found for which the behaviour of K_1 does not closely resemble that of Δ_{K-K_1}.)

A stochastically perturbed single wave has been proposed as a model for diffusive transport due to breaking Rossby waves (Bowman 1995). Our results, however, suggest that while such a model will, for finite times, yield faster mixing than will the unperturbed single wave, this will not be the case for the two-wave model. Transport is much stronger in the stochastically perturbed single-wave model than in the deterministic two-wave model (cf. figure 13); but mixing is weaker (cf. figure 15). The effects of chaotic advection cannot be captured by stochasticity alone. (It must be emphasized that we have considered only weak stochasticity, in the sense that the

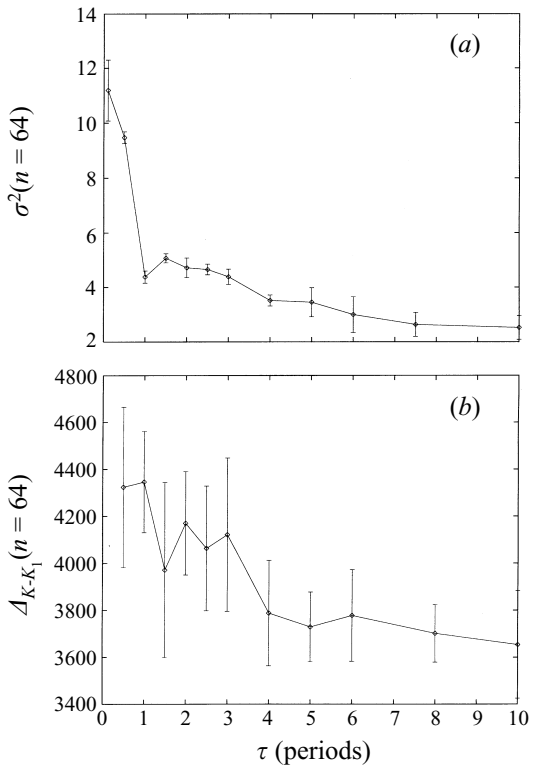

FIGURE 23. Variation of (*a*) $\sigma^2(n = 64)$ and (*b*) $\Delta_{K-K_1}(n = 64)$ with τ for a stochastically perturbed single wave, with $c_0 = 3$ and $\delta_c = 0.1$. The initial distribution consists of 33 709 points inside $f(L_{2,1}(1))$ (for $\varepsilon = 0.1$). The average values are determined from an ensemble of eight realizations; the error bars are given by the standard deviation. In (*b*), the spectrum is computed using interparticle separations from 0 to 20 on a grid of 100 000 points.

streamline topology is only slightly disturbed. The results may be quite different for strong stochasticity (cf. Liu, Muzzio & Peskin 1994).)

7. Discussion

7.1. *Summary*

In this paper, we have derived and analysed a new model of chaotic mixing and transport in Rossby-wave critical layers. This work was motivated by the problem of dynamical consistency in previous two-wave models and by the need for a quantitative characterization of mixing and transport. The Stewartson–Warn–Warn solution from Rossby-wave critical-layer theory has been used to derive a model that is dynamically consistent to leading order in the wave amplitudes, and several quantitative diagnostics have been used to characterize mixing and transport separately.

The rate and spatial extent of transport have been characterized with lobe dynamics (figure 6) and the mean-square dispersion (figure 9), respectively. Initial distributions bounded by the perturbed and unperturbed separatrices have been used. It has been found that the time evolution of the transport fluxes depends on the location of the initial distribution relative to the turnstile (i.e. the perturbed separatrix). For initial distributions located entirely to one side of the turnstile, there are two power-

law decay regimes; for an initial distribution straddling the turnstile, there is only one. Regarding the spatial extent of transport, the mean-square dispersion initially increases but is approximately independent of n for large n. The initial rate of increase is much greater for a distribution straddling the turnstile than for one located entirely to one side of it. The saturation of the mean-square dispersion is a consequence of the phase-space geometry of 1.5 degree-of-freedom Hamiltonian systems: invariant tori are barriers to transport. These results underscore the importance of the initial tracer distribution and the markedly non-diffusive nature of transport in the two-wave model; they are also consistent with numerical calculations of stratospheric tracer trajectories (Schoeberl & Bacmeister 1993).

Mixing has been characterized by isotropic power spectra of the interparticle spacing (figure 10). The first two moments of the spectra have been used as proxies for mixing (figure 11). They clearly demonstrate that mixing in the two-wave model is a two-step process: small scales are developed first, and homogenized later. The lack of homogenization in the unperturbed $\varepsilon = 0$ (pure stirring) case is striking.

The parameter dependence of mixing and transport has been examined with a Melnikov analysis as the starting point. A Melnikov analysis is applicable to transport inasmuch as it describes the phase-space transport in the vicinity of the the perturbed separatrix; however, it does not take the initial tracer distribution into account and, as such, contains no information about its time development. This is highlighted by figure 14(b). In addition, while the Melnikov analysis predicts that the mean-square dispersion varies linearly with ε, we find a strongly nonlinear (although monotonic) dependence (figure 13). With respect to mixing (figure 15), direct numerical computations indicate that the mixing (up to a given time) is not a monotonic function of ε. As is consistent with previous studies (cf. Aref & Balachandar 1986), the mixing is optimized for a particular value of the perturbation. We have argued that the existence of an optimal value of ε is a consequence of a balance between two competing effects. As ε increases, both the stretching rates and the area of the chaotic region increase; however, the stretching rates rapidly saturate with ε (figure 16), causing the mixing to decrease beyond a certain point. These mixing results are in marked contrast to what would be predicted by typical parameterizations. With a mixing-length type parameterization (e.g. Tennekes & Lumley 1972), the eddy flux is an increasing (in fact quadratic) function of the eddy amplitude.

We have investigated the robustness of these results by introducing multiplicative noise. (To be precise, the phase speed of the transient wave has been stochastically perturbed.) One expects that stochasticity and chaotic advection should have roughly similar effects. This has indeed been observed, though with some notable caveats. Provided that the stochasticity is sufficiently weak and the transient (chaotic) perturbation sufficiently strong, there is the same general behaviour (figure 20): for finite times, transport increases and mixing decreases as the stochasticity increases (i.e. as the autocorrelation time of the multiplicative noise is reduced). Despite the fact that the system is non-periodic, the nature of the mixing does indeed inherit something from the underlying chaotic mixing. The decrease in the mixing is largely a result of a decrease in the ensemble-averaged finite-time Liapunov exponent caused by the stochastic perturbation (figure 21); similar behaviour in the diagnostics and the spectra is observed for a stochastically perturbed single-wave model, in which mixing is generated purely by stochasticity (figure 23). The main difference in this case is that the mean-square dispersion is a quasi-monotonic function of the autocorrelation time.

7.2. *Physical applicability*

We now wish to discuss the physical applicability of our model. We expect that it should be of use in the stratospheric context because the SWW solution, upon which it is based, is thought to be a useful conceptual model of Rossby-wave breaking in the stratosphere. A number of recent studies (e.g. Pierce & Fairlie 1993; Bowman 1993; Waugh *et al.* 1994) have shown that chaotic advection takes place around the polar vortex though a precise physical mechanism has yet to be identified. Our model postulates that chaotic advection in the stratospheric polar vortex results from interactions between a stationary wave and a transient wave. While this is a very crude model, there is some observational support for it (see e.g. Manney, Farrara & Mechoso 1991). The nonlinear interactions between stationary and transient waves also play a central role in the numerical study of Salby (1992). The principal result of Salby's study, that eddy transport increases when the critical lines of the stationary and transient waves are close together, is entirely consistent with ours. Stationary–transient interactions are also present in numerical simulations of a barotropically unstable circumpolar vortex (e.g. Ishioka & Yoden 1995).

Despite its highly simplified nature, the model does capture several important features seen in recent studies of stratospheric mixing and transport. There are barriers to transport. There are regions where mixing is strong and homogenization rapid, as well as regions where mixing is weak and there is only filamentation. Most importantly, the model captures the crucial idea that mixing and transport are markedly non-diffusive, and that their time evolution is very dependent on the initial tracer distribution.

The fact that the development of small scales is a precondition of mixing implies that models with insufficient development (and resolution) of small scales will require unrealistically large diffusivities in order to attain a given flux. This has particularly serious implications for applications to atmospheric chemistry (see e.g. Pierrehumbert & Yang 1993). One of the major problems with present-day atmospheric and (especially) oceanic general circulation models is their excessive diffusivity.

One problem that could limit the model's physical applicability is the shear instability of the SWW solution (Killworth & McIntyre 1985). The instability has its origin in the wrap-up of the vorticity contours, and its effects are quite violent in the SWW limit. However, for finite μ, μ being the ratio of the natural length scale to the wavelength of the solution, the cat's eye structure persists (Haynes 1989): the shear instability is suppressed by straining from the background flow (Dritschel *et al.* 1991). This straining should be even stronger in chaotic regions. (Moreover, because of the time-dependent northern boundary condition of the two-wave model, the instability should be weaker than for the SWW solution.) Even if the instability were to occur, it would likely be spatially localized and it will of course saturate; thus, it may not have much effect on mixing and transport. Failing that, the instability could, possibly, be parameterized as a stochastic forcing.

Notwithstanding this, objections to the model could be raised on the basis that the assumptions required by the SWW solution are so stringent that few real flows would satisfy them. Still, the physical mechanism underlying the SWW solution – that advection by waves is as important as advection by the basic state and that there exist cat's eyes with stagnation points and closed streamlines – is robust and should extend beyond the model's formal range of validity. It has been observed in contour advection calculations (e.g. Norton 1994; Waugh & Plumb 1994) that the development of small scales depends mainly on the large-scale flow; this is

precisely the viewpoint that we have tried to formalize in the derivation of our model.

Apart from the stratospheric context, chaotic mixing and transport in the presence of a non-zero potential vorticity gradient may be relevant to other geophysical situations where, as in our case, the flow in one (inner) region is essentially kinematic and determined by the dynamics in another (outer) region. A possible example is the oceanic Gulf Stream, where the upper-level potential-vorticity gradients are much stronger than the lower-level gradients (Bower & Lozier 1994). It is conceivable that, driven by disturbances in the upper (near-surface) levels of the Gulf Stream, chaotic mixing and transport could occur in the lower levels. This situation is reminiscent of weakly nonlinear baroclinic instability in the two-layer quasi-geostrophic model (Warn & Gauthier 1989).

The authors would like to thank P. H. Haynes and an anonymous referee for many helpful suggestions which greatly improved the presentation of the material. Helpful comments were also received from D. del-Castillo-Negrete and J. B. Weiss. K.N. acknowledges receipt of a postgraduate scholarship from the Natural Sciences and Engineering Research Council of Canada. T.G.S. acknowledges grant support from NSERC and from the Atmospheric Environment Service of Canada.

Appendix A. The SWW solution

A brief derivation of the SWW solution following Stewartson (1978) and Killworth & McIntyre (1985) is presented. SWW begin with the barotropic vorticity equation for inviscid incompressible flow on the β-plane,

$$\frac{\mathrm{D}q}{\mathrm{D}t} = 0, \tag{A 1}$$

where $q = \beta y + \nabla^2\psi$ is (to within a constant) the absolute vorticity, ψ is the stream function, and $\mathrm{D}/\mathrm{D}t = \partial/\partial t + \partial(\psi, \cdot)$ is the material derivative. Taking the basic state to be a linear shear flow $U = \Lambda y$, and assuming the perturbation amplitude ϵ to be small,

$$\psi = -\tfrac{1}{2}\Lambda y^2 + \epsilon\phi(x, y, t). \tag{A 2}$$

Scaling length by Λ/β, time by Λ^{-1}, and ϕ by Λ^3/β^2, (A 1) becomes

$$\nabla^2\phi_t + y\nabla^2\phi_x + \phi_x + \epsilon(\phi_x\nabla^2\phi_y - \phi_y\nabla^2\phi_x) = 0.$$

Assuming that the x-wavelength $2\pi/m$ of the solutions is much greater than the natural lengthscale Λ/β, i.e.

$$\mu = \frac{\Lambda m}{\beta} \ll 1, \tag{A 3}$$

then to leading order in μ,

$$\left(\frac{\partial}{\partial t} + y\frac{\partial}{\partial x}\right)\frac{\partial^2\phi}{\partial y^2} - \epsilon\left(\frac{\partial\phi}{\partial x}\frac{\partial^3\phi}{\partial y^3} - \frac{\partial\phi}{\partial y}\frac{\partial^3\phi}{\partial x\partial y^2}\right) + \frac{\partial\phi}{\partial x} = 0 \tag{A 4}$$

after rescaling x and t by μ. Thus t is now a slow time and x is now a stretched variable; the solutions have a small aspect ratio (i.e. the critical layer is very narrow).

It can be shown that the leading-order approximation to the linear solution of (A 4) is steady for $t \gg 1$. At times $t = O(\epsilon^{-1/2})$, however, the linear solution breaks

down within a critical layer of thickness $O(\epsilon^{1/2})$. The nonlinear evolution (for $y \neq 0$) is then given by

$$\phi = 2A(x,\tau) \mid y \mid^{1/2} K_1\big(2 \mid y \mid^{1/2}\big), \quad y < 0\,,$$
$$\phi = B(x,\tau)y^{1/2}J_1(2y^{1/2}) + C(x,\tau)y^{1/2}Y_1(2y^{1/2}), \quad y > 0\,,$$

where A, B, C are functions to be determined, J_1, K_1, Y_1 are Bessel functions, and $\tau = \epsilon^{1/2}t$. The functions A, B, C must obey matching conditions across the critical layer (i.e. between the nonlinear critical layer and the linear outer region). From the matching conditions, the northern boundary condition may be re-expressed as

$$-\pi A(x,\tau)Y_1(2y_o^{1/2}) + B(x,\tau)J_1(2y_o^{1/2}) = a\frac{\cos x}{y_o^{1/2}}\,. \tag{A 5}$$

To obtain an equation for the critical-layer evolution, a stretched variable $Y = \epsilon^{-1/2}y$ is introduced. Writing the perturbation stream function as

$$\phi = A(x,\tau)\big[1 - \tfrac{1}{2}Y\epsilon^{1/2}(\log\epsilon + 4\gamma - 2)\big] + \epsilon^{1/2}\Psi(x,\tau,Y) + O(\epsilon\log\epsilon),$$
$$\frac{\partial^2\Psi}{\partial Y^2} = \zeta_1(x,\tau,Y)\,,$$

where γ is Euler's constant, and $\zeta_1(x,\tau,Y)$ is the leading-order approximation to the scaled relative vorticity $\nabla^2\phi$ inside the critical layer, SWW show that

$$\frac{\partial\zeta_1}{\partial\tau} + Y\frac{\partial\zeta_1}{\partial x} + \frac{\partial A}{\partial x}\frac{\partial\zeta_1}{\partial Y} + \frac{\partial A}{\partial x} = 0. \tag{A 6}$$

The SWW solution is obtained from (A 6) with one final approximation – that the response be monochromatic. Although the forcing is monochromatic, the response need not be so in general; in the large-τ limit, however, it is not unreasonable to expect that there will be a steady monochromatic response. Therefore, SWW choose the northern boundary position y_o such that $A(x,\tau)$ is independent of τ. With

$$J_1(2y_o^{1/2}) = 0, \qquad Y_1(2y_o^{1/2}) \neq 0\,, \tag{A 7}$$

and an appropriate choice of a, it follows from (A 5) that the response is indeed monochromatic, namely

$$A(x) = \cos x\,.$$

This yields

$$\left\{\frac{\partial}{\partial\tau} - \frac{\partial\Psi_0}{\partial Y}\frac{\partial}{\partial x} + \frac{\partial\Psi_0}{\partial x}\frac{\partial}{\partial Y}\right\}q = 0, \tag{A 8}$$

where $q = Y + \zeta_1$ is the first approximation to the (scaled) absolute vorticity in the critical layer and the advecting stream function Ψ_0 is given by

$$\Psi_0 = -\tfrac{1}{2}Y^2 + \cos x. \tag{A 9}$$

According to (A 8), the q-field is wrapped up by the cat's eye structure (A 9) like "spaghetti on a fork" (Killworth & McIntyre 1985; cf. figure 2*a*).

Appendix B. Lobe dynamics fluxes for the two-wave model

In this Appendix, we sketch the derivation of the lobe dynamics fluxes (3.1)–(3.2).

Defining $L_{k,j}(n)$ to be the lobe that carries tracers from region k to region j on the nth iterate of the Poincaré map (Wiggins 1992, theorem 2.5):

$$a_{i,j}(n) = \sum_{k=1}^{N_R} \left[\mu\left(L^i_{k,j}(n) \right) - \mu\left(L^i_{j,k}(n) \right) \right], \tag{B 1}$$

where N_R denotes the number of regions. The area of the lobe $L_{k,j}(n)$, i.e. $\mu\big(L_{k,j}(n)\big)$, can be evaluated using (Wiggins 1992, theorem 2.6):

$$\mu\left(L^i_{k,j}(n) \right) = \sum_{s=1}^{N_R} \sum_{l=0}^{n-1} \mu\left(L_{k,j}(1) \bigcap f^l\left(L_{i,s}(1) \right) \right) - \sum_{s=1}^{N_R} \sum_{l=1}^{n-1} \mu\left(L_{k,j}(1) \bigcap f^l\left(L_{s,i}(1) \right) \right). \tag{B 2}$$

We illustrate this procedure for $a_{1,2}(n)$. Applying (B 1),

$$\begin{aligned} a_{1,2}(n) &= \sum_{k=1}^{3} \left[\mu\left(L^1_{k,2}(n) \right) - \mu\left(L^1_{2,k}(n) \right) \right] \\ &= \mu\left(L^1_{1,2}(n) \right) - \mu\left(L^1_{2,1}(n) \right) + \mu\left(L^1_{3,2}(n) \right) - \mu\left(L^1_{2,3}(n) \right), \end{aligned} \tag{B 3}$$

where we have used the fact that $L_{1,1}(n) = L_{2,2}(n) = \emptyset$ by definition. From (B 2),

$$\begin{aligned} \mu\left(L^1_{1,2}(n) \right) &= \sum_{s=1}^{3} \sum_{l=0}^{n-1} \mu\left(L_{1,2}(1) \bigcap f^l\left(L_{1,s}(1) \right) \right) - \sum_{s=1}^{3} \sum_{l=1}^{n-1} \mu\left(L_{1,2}(1) \bigcap f^l\left(L_{s,1}(1) \right) \right) \\ &= \sum_{l=0}^{n-1} \mu\left(L_{1,2}(1) \bigcap f^l\left(L_{1,2}(1) \right) \right) - \sum_{l=1}^{n-1} \mu\left(L_{1,2}(1) \bigcap f^l\left(L_{2,1}(1) \right) \right), \end{aligned}$$

where we have used $L_{1,3}(n) = L_{3,1}(n) = \emptyset$. Simplifying the last equation,

$$\mu\left(L^1_{1,2}(n) \right) = \mu\left(L_{1,2}(1) \right) + \sum_{l=1}^{n-1} \left[\mu\left(L_{1,2}(1) \bigcap f^l\left(L_{1,2}(1) \right) \right) - \mu\left(L_{1,2}(1) \bigcap f^l\left(L_{2,1}(1) \right) \right) \right].$$

Repeating this procedure for the other terms in (B 3), one then obtains

$$\begin{aligned} a_{1,2}(n) = \mu\left(L_{1,2}(1) \right) + \sum_{l=1}^{n-1} \Bigg[& \mu\left(L_{1,2}(1) \bigcap f^l\left(L_{1,2}(1) \right) \right) - \mu\left(L_{1,2}(1) \bigcap f^l\left(L_{2,1}(1) \right) \right) \\ & + \mu\left(L_{2,1}(1) \bigcap f^l\left(L_{2,1}(1) \right) \right) - \mu\left(L_{2,1}(1) \bigcap f^l\left(L_{1,2}(1) \right) \right) \\ & + \mu\left(L_{3,2}(1) \bigcap f^l\left(L_{1,2}(1) \right) \right) - \mu\left(L_{3,2}(1) \bigcap f^l\left(L_{2,1}(1) \right) \right) \\ & + \mu\left(L_{2,3}(1) \bigcap f^l\left(L_{2,1}(1) \right) \right) - \mu\left(L_{2,3}(1) \bigcap f^l\left(L_{1,2}(1) \right) \right) \Bigg]. \end{aligned} \tag{B 4}$$

$a_{2,3}(n)$ and $a_{1,3}(n)$ can be calculated similarly.

Conservation of area and conservation of species may be written as

$$\sum_{i=1}^{N_R} a_{i,j}(n) = 0 \quad \text{and} \quad \sum_{j=1}^{N_R} a_{i,j}(n) = 0, \tag{B 5}$$

respectively. It then follows that

$$a_{2,1}(n) + a_{3,1}(n) = a_{1,2}(n) + a_{1,3}(n), \quad a_{1,3}(n) + a_{2,3}(n) = a_{3,1}(n) + a_{3,2}(n). \tag{B 6}$$

Thus if $a_{1,3}(n) = a_{3,1}(n) = 0$, which is approximately the case when the lower separatrix splitting is small,

$$a_{1,2}(n) = a_{2,1}(n), \quad a_{2,3}(n) = a_{3,2}(n). \tag{B 7}$$

In other systems, some of the turnstile intersections are identically zero; we have retained all the terms in (B 4). With periodic boundary conditions, all turnstile intersections are, at least in principle, possible. When the domain is spatially unbounded, some intersections (e.g. self-intersections) do not occur because lobes no longer wrap up. By analogy with the oscillating vortex pair flow of RLW (see Wiggins 1992, §2.4), it can then be shown that

$$\begin{aligned}\mu\left(L^1_{2,1}(n)\right) &= \sum_{l=1}^{n-1}\left[\mu\left(L_{2,1}(1)\bigcap f^l\left(L_{1,2}(1)\right)\right) - \mu\left(L_{2,1}(1)\bigcap f^l\left(L_{2,1}(1)\right)\right)\right] \\ &= 0\end{aligned} \tag{B 8}$$

for an unbounded domain. In words, tracers that escape from region 1 into region 2 never return. This would imply irreversible transport of species 1 into region 2, something that does not occur for periodic boundary conditions.

REFERENCES

Aref, H. 1984 Stirring by chaotic advection *J. Fluid Mech.* **143**, 1–21.

Aref, H. 1991 Stochastic particle motion in laminar flows. *Phys. Fluids* A **3**, 1009–1016.

Aref, H. & Balachandar, S. 1986 Chaotic advection in a Stokes flow. *Phys. Fluids* **29**, 3515-3520.

Aref, H. & Jones, S. W. 1989 Enhanced separation of diffusing particles by chaotic advection. *Phys. Fluids* A **1**, 470–474.

Bacmeister, J. T., Eckermann, S. D., Newman, P.A., *et al.* 1996 Stratospheric horizontal wavenumber spectra of winds, potential temperature, and atmospheric tracers observed by high-altitude aircraft. *J. Geophys. Res.* **101,** 9441–9470.

Bower, A. S. & Lozier, M. S. 1994 A closer look at particle exchange in the Gulf Stream. *J. Phys. Oceanogr.* **24**, 1399–1418.

Bowman, K. P. 1993 Large-scale isentropic mixing properties of the Antarctic polar vortex from analyzed winds. *J. Geophys. Res.* **98**, 23013–23027.

Bowman, K. P. 1995 Diffusive transport by breaking waves. *J. Atmos. Sci.* **52**, 2416–2417.

Bowman, K. P. 1996 Rossby wave phase speeds and mixing barriers in the stratosphere, Part 1: observations. *J. Atmos. Sci.* **53**, 905–916.

Chaiken, J., Chevray, R., Tabor, M. & Tan, Q. M. 1986 Experimental study of Lagrangian turbulence in Stokes flow. *Proc. R. Soc. Lond.* A **408**, 165–174.

Corrsin, S. 1974 Limitations of gradient transport models in random walks and in turbulence. *Adv. Geophys.* **18A**, 25–71.

Cox, S. M., Drazin, P. G., Ryrie, S. C. & Slater, K. 1990 Chaotic advection of irrotational flows and of waves in fluids. *J. Fluid Mech.* **214**, 517–534.

Del-Castillo-Negrete, D. & Morrison, P. J. 1993 Chaotic transport by Rossby waves in shear flow. *Phys. Fluids* A **5**, 948–965 (referred to herein as DM).

Drazin, P. G. 1992 *Nonlinear Systems.* Cambridge University Press.

Dritschel, D. G., Haynes, P. H., Juckes, M. N. & Shepherd, T. G. 1991 The stability of a two-dimensional vorticity filament under uniform strain. *J. Fluid Mech.* **230**, 647–665.

Dutta, P. & Chevray, R. 1995 Inertial effects in chaotic mixing with diffusion. *J. Fluid Mech.* **285**, 1–16.

Franjione, J. G. & Ottino, J. M. 1987 Feasibility of numerical tracking of material lines and surfaces in chaotic flows. *Phys. Fluids* **30**, 3641–3643.

Gilbert, A. D. 1988 Spiral structures and spectra in two-dimensional turbulence. *J. Fluid Mech.* **193**, 475–497.

Haynes, P. H. 1989 The effect of barotropic instability on the nonlinear evolution of a Rossby-wave critical layer. *J. Fluid Mech.* **207**, 231–266.

Ishioka, K. & Yoden, S. 1995 Non-linear aspects of a barotropically unstable polar vortex in a forced-dissipative system: flow regimes and tracer transport. *J. Met. Soc. Japan* **73**, 201–212.

Jana, S. C., Metcalfe, G. & Ottino, J. M. 1994 Experimental and computational study of mixing in complex Stokes flow: the vortex mixing flow and multicellular cavity flows. *J. Fluid Mech.* **269**, 199–246.

Juckes, M. N. & McIntyre, M. E. 1987 A high-resolution one-layer model of breaking planetary waves in the stratosphere. *Nature* **328**, 590–596.

Kampen, N. G. van 1981 *Stochastic Processes in Physics and Chemistry*. North-Holland.

Killworth, P. D. & McIntyre, M. E. 1985 Do Rossby-wave critical layers absorb, reflect or over-reflect? *J. Fluid Mech.* **161**, 449–492.

Lesieur, M. 1990 *Turbulence in Fluids*, 2nd Edn. Kluwer.

Lichtenberg, A. J. & Lieberman, M. A. 1992 *Regular and Chaotic Dynamics*, 2nd Edn. Springer.

Liu, M., Muzzio, F. J. & Peskin, R. L. 1994 Quantification of mixing in aperiodic chaotic flows. In *Chaos Applied to Fluid Mixing* (ed. H. Aref & M. S. El Naschie), pp. 125–149, Pergamon.

MacKay, R. S. & Meiss, J. D. 1987 (Eds.) *Hamiltonian Dynamical Systems*. Adam Hilger.

Manney, G. L., Farrara, J. D. & Mechoso, C. R. 1991 The behavior of wave 2 in the southern hemisphere stratosphere during late winter and early spring. *J. Atmos. Sci.* **48**, 976–998.

Maslowe, S. A. 1986 Critical layers in shear flows. *Ann. Rev. Fluid Mech.* **18**, 405–432.

McIntyre, M. E. 1989 On the Antarctic ozone hole. *J. Atmos. Terr. Phys.* **51**, 29–43.

McIntyre, M. E. 1992 Atmospheric dynamics: some fundamentals, with observational implications. In *The Use of EOS for Studies of Atmospheric Physics* (ed. J. C. Gille & G. Visconti), pp. 313–486. North-Holland.

McIntyre, M. E. & Palmer, T. N. 1983 Breaking planetary waves in the stratosphere. *Nature* **305**, 593–600.

McLachlan, R. I. 1995 On the numerical integration of ordinary differential equations by symmetric composition methods. *SIAM J. Sci. Comput.* **16**, 151–168.

Mezić, I. & Wiggins, S. 1994 On the dynamical origin of asymptotic t^2 dispersion of a nondiffusive tracer in incompressible laminar flows. *Phys. Fluids* **6**, 2227–2229.

Moss, F., Bulsara, A. & Shlesinger, M. F. 1993 (Eds.) *Proceedings of the NATO Advanced Research Workshop, Stochastic Resonance in Physics and Biology. J. Statist. Phys.* **70**, 1–514.

Muzzio, F. J., Meneveau, C., Swanson, P. D. & Ottino, J. M. 1992 Scaling and multifractal properties of mixing in chaotic flows. *Phys. Fluids* A **4**, 1439–1456.

Muzzio, F. J., Swanson, P. D. & Ottino, J. M. 1991 The statistics of stretching and stirring in chaotic flows. *Phys. Fluids* A **3**, 822–834.

Norton, W. A. 1994 Breaking Rossby waves in a model stratosphere diagnosed by a vortex-following coordinate system and a technique for advecting material contours. *J. Atmos. Sci.* **51**, 654–673.

Ottino, J. M. 1989 *The Kinematics of Mixing: Stretching, Chaos and Transport*. Cambridge University Press.

Parker, T. S. & Chua, L. O. 1992 *Practical Numerical Algorithms for Chaotic Systems*. Springer.

Pedlosky, J. 1987 *Geophysical Fluid Dynamics*, 2nd Edn. Springer.

Pierce, R. B. & Fairlie, T. D. A. 1993 Chaotic advection in the stratosphere: implications for the dispersal of chemically perturbed air from the polar vortex. *J. Geophys. Res.* **98**, 18589–18595.

Pierrehumbert, R. T. 1991*a* Large-scale horizontal mixing in planetary atmospheres. *Phys. Fluids* A **3**, 1250–1260.

Pierrehumbert, R. T. 1991*b* Chaotic mixing of tracer and vorticity by modulated traveling Rossby waves. *Geophys. Astrophys. Fluid Dyn.* **58**, 285–319.

Pierrehumbert, R. T. 1992 Spectra of tracer distributions: a geometric approach. In *Nonlinear Phenomena in Atmospheric and Oceanic Sciences* (ed. G. F. Carnevale & R. T. Pierrehumbert), pp. 27–46. Springer.

Pierrehumbert, R. T. 1994 Tracer microstructure in the large-eddy dominated regime. In *Chaos Applied to Fluid Mixing* (ed. H. Aref & M. S. El Naschie), pp. 347–366. Pergamon.

Pierrehumbert, R. T. & Yang, H. 1993 Global chaotic mixing on isentropic surfaces. *J. Atmos. Sci.* **50**, 2462–2480.

Polvani, L. M. & Plumb, R. A. 1992 Rossby wave breaking, microbreaking, filamentation and secondary vortex formation: the dynamics of a perturbed vortex. *J. Atmos. Sci.* **49**, 462–476.

Polvani, L. M., Waugh, D. W. & Plumb, R. A. 1995 On the subtropical edge of the stratospheric surf zone. *J. Atmos. Sci.* **52**, 1288–1309.

Polvani, L. M. & Wisdom, J. 1990 Chaotic Lagrangian trajectories around an elliptical vortex patch embedded in a constant and uniform background shear flow. *Phys. Fluids* A **2**, 123–126.

Rom-Kedar, V. 1994 Homoclinic tangles – classification and applications. *Nonlinearity* **7**, 441–473.

Rom-Kedar, V., Leonard, A. & Wiggins, S. 1990 An analytical study of transport, mixing and chaos in an unsteady vortical flow. *J. Fluid Mech.* **246**, 347–394 (referred to herein as RLW).

Saffman, P. G. 1971 On the spectrum and decay of random two-dimensional vorticity distributions at large Reynolds number. *Stud. Appl. Maths* **50**, 377–383.

Salby, M. L. 1992 The influence of planetary-wave transience on horizontal air motions in the stratosphere. *J. Atmos. Sci.* **49**, 405–421.

Samelson, R. M. 1992 Fluid exchange across a meandering jet. *J. Phys. Oceanogr.* **22**, 431–442.

Samelson, R. M. 1996 Chaotic transport by mesoscale motions. In *Stochastic Modelling and Physical Oceanography* (ed. R. J. Adler, P. Müller & B. Rozovskii), pp. 423–438. Birkhäuser.

Schoeberl, M. L. & Bacmeister, J. T. 1993 Mixing processes in the extra-tropical stratosphere. In *The Role of the Stratosphere in Global Change* (ed. M.-L. Chanin), pp. 135–152. Springer.

Sirovich, L., Everson, R. & Manin, D. 1995 Turbulent spectrum of the Earth's ozone field. *Phys. Rev. Lett.* **74**, 2611–2614.

Stewartson, K. 1978 The evolution of the critical layer of a Rossby wave. *Geophys. Astrophys. Fluid Dyn.* **9**, 185–200.

Stewartson, K. 1981 Marginally stable inviscid flows with critical layers. *IMA J. Appl. Maths* **27**, 133–175.

Strahan, S. E. & Mahlman, J. D. 1994 Evaluation of the SKYHI general circulation model using aircraft N_2O measurements. Part 2. Tracer variability and diabatic meridional circulation. *J. Geophys. Res.* **99,** 10319–10332.

Tennekes, H. & Lumley, J. L. 1972 *A First Course in Turbulence*. MIT Press.

Városi, F., Antonsen, T.M. & Ott, E. 1991 The spectrum of fractal dimensions of passively convected scalar gradients in chaotic fluid flows. *Phys. Fluids* A **3,** 1017–1028.

Warn, T. & Gauthier, P. 1989 Potential vorticity mixing by marginally unstable baroclinic disturbances. *Tellus* **41A**, 115–131.

Warn, T. & Warn, H. 1978 The evolution of a nonlinear critical layer. *Stud. Appl. Maths* **59**, 37–71.

Waugh, D. W. & Plumb, R. A. 1994 Contour advection with surgery: a technique for investigating fine-scale structure in tracer transport. *J. Atmos. Sci.* **51**, 530–540.

Waugh, D. W., Plumb, R. A., Atkinson, R. J., *et al.* 1994 Transport out of the lower stratospheric Arctic vortex by Rossby wave breaking. *J. Geophys. Res.* **99**, 1071–1088.

Weiss, J. B. 1991 Transport and mixing in traveling waves. *Phys. Fluids* A **3**, 1379–1384.

Weiss, J. B. & Knobloch, E. 1989 Mass transport by modulated traveling waves. *Phys. Rev.* A **42**, 2579–2589.

Wiggins, S. 1988 Stirred but not mixed. *Nature* **333**, 395–396.

Wiggins, S. 1990 *Introduction to Applied Nonlinear Dynamical Systems and Chaos*. Springer.

Wiggins, S. 1992 *Chaotic Transport in Dynamical Systems*. Springer.

Yoshida, H. 1990 Construction of higher order symplectic integrators. *Physica* D **150**, 262–268.

Young, W. R. 1988 Arrested shear dispersion and other models of anomalous diffusion. *J. Fluid Mech.* **193**, 129–149.